WATER RESOURCES RESEARCH, VOL. 46, W06507, doi:10.1029/2009WR007811, 2010

Click Here for Full Article

Evaluation of the Global Land Data Assimilation System using global river discharge data and a source-to-sink routing scheme

Benjamin F. Zaitchik,[1] Matthew Rodell,[2] and Francisco Olivera[3]

Received 2 February 2009; revised 26 September 2009; accepted 31 December 2009; published 10 June 2010.

[1] Advanced land surface models (LSMs) offer detailed estimates of distributed hydrological fluxes and storages. These estimates are extremely valuable for studies of climate and water resources, but they are difficult to verify as field measurements of soil moisture, evapotranspiration, and surface and subsurface runoff are sparse in most regions. In contrast, river discharge is a hydrologic flux that is recorded regularly and with good accuracy for many of the world's major rivers. These measurements of discharge spatially integrate all upstream hydrological processes. As such, they can be used to evaluate distributed LSMs, but only if the simulated runoff is properly routed through the river basins. In this study, a rapid, computationally efficient source-to-sink (STS) routing scheme is presented that generates estimates of river discharge at gauge locations based on gridded runoff output. We applied the scheme as a postprocessor to archived output of the Global Land Data Assimilation System (GLDAS). GLDAS integrates satellite and ground-based data within multiple offline LSMs to produce fields of land surface states and fluxes. The application of the STS routing scheme allows for evaluation of GLDAS products in regions that lack distributed in situ hydrological measurements. We found that the four LSMs included in GLDAS yield very different estimates of river discharge and that there are distinct geographic patterns in the accuracy of each model as evaluated against gauged discharge. The choice of atmospheric forcing data set also had a significant influence on the accuracy of simulated discharge.

Citation: Zaitchik, B. F., M. Rodell, and F. Olivera (2010), Evaluation of the Global Land Data Assimilation System using global river discharge data and a source-to-sink routing scheme, *Water Resour. Res.*, *46*, W06507, doi:10.1029/2009WR007811.

1. Introduction

[2] Rivers are the ultimate integrators of watershed hydrology. The imprints of upstream climate variability, land surface and subsurface processes, and human modifications to the hydrological system are all present in a river hydrograph, making a gauged measurement of discharge one of the most integrative observations available to landscape-scale hydrology. In situ measurements of precipitation, evaporation, soil moisture, or groundwater reflect only the local conditions. River discharge is also a historically well-monitored hydrological flux. River gauge records are available for decades for many of the world's major rivers and they typically provide reliable information, with accuracy of up to 5% [*Dingman*, 2001], and generally in the range of 10–20% [*Fekete et al.*, 2002].

[3] The duration, reliability, and integrative nature of river gauge measurements underscore their utility in the calibration and evaluation of Earth system models. In a number of studies, river gauge data have been used to assess the applicability of general circulation models [e.g., *Arora et al.*, 1999; *Ducharne et al.*, 2003; *Miller et al.*, 1994], atmospheric and meteorological reanalyses [e.g., *Dai and Trenberth*, 2002; *Ngo-Duc et al.*, 2005], and surface hydrological models [e.g., *Decharme et al.*, 2008; *Oki et al.*, 1999; *Voisin et al.*, 2008]. Such studies demonstrate an obvious complementarity between gauge measurements and distributed models: the gauge data provide a reliable measurement of basin-net hydrological flux, while the model simulates multiple surface and/or atmospheric processes distributed over the basin. Gauge data offer a means for assessing model performance, while the model explains, and, potentially, predicts variability in gauged river discharge.

[4] In order to realize fully this complementarity, it is necessary to implement a runoff routing scheme that transports runoff simulated at each model grid cell to the drainage location that corresponds to the in situ gauge. A number of routing schemes exist, and they vary widely in their complexity and degree of calibration. For water management applications on the watershed scale, highly parameterized, geographically specific models can be used to provide accurate estimates of streamflow and reservoir status [e.g., *Zagona et al.*, 2001]. For global-scale applications, however, computationally efficient, easily parameterized routing methodologies are preferable.

[5] In an early and influential effort at large-scale routing, *Vorosmarty et al.* [1989] prepared a river routing network for the Amazon basin at 0.5° resolution. Runoff produced by a water balance approach was routed through the network

[1]Department of Earth and Planetary Sciences, Johns Hopkins University, Baltimore, Maryland, USA.
[2]Hydrological Sciences Branch, NASA Goddard Space Flight Center, Greenbelt, Maryland, USA.
[3]Zachry Department of Civil Engineering, Texas A&M University, College Station, Texas, USA.

Copyright 2010 by the American Geophysical Union.
0043-1397/10/2009WR007811

using a linear transfer model, with flow time calculated as a function of flow length, estimated subgrid-scale sinuosity, and grid-scale velocities estimated on the basis of mean downstream discharge [after *Leopold et al.*, 1964]. A similar linear transfer model was adopted by *Miller et al.* [1994] for application to the Goddard Institute for Space Studies (GISS) General Circulation Model (GCM) at global scale. In their formulation, runoff produced by a GCM at 4° × 5° was routed to the ocean through a 2° × 2.5° network in which flow direction was determined by topography and velocity was a function of slope. Because the scale of implementation was quite coarse, slope-based estimates of velocity were intentionally calculated to yield low values, providing an implicit correction for subgrid-scale sinuosity and the time it would realistically take runoff to work its way through the river system. *Sausen et al.* [1994] implemented a linear routing scheme for the European Center Hamburg (ECHAM) GCM, with transport parameters semiobjectively calibrated to match observed flow in major gauged rivers. In a study of the Amazon River system *Costa and Foley* [1997] largely adopted the velocity estimation procedure of *Miller et al.* [1994]. As a refinement, they estimated the sinuosity coefficient independently for each tributary within the Amazon basin, and they adjusted velocities as a function of stream order. *Costa and Foley* [1997] further divided runoff into surface and subsurface components and applied differential source retention times to each. Further variants on the *Miller et al.* [1994] approach include the global hydrological routing algorithm (HYDRA [*Coe*, 2000]), which was implemented at 5′ resolution, included variability in surface waters, and made some adjustments to the *Miller et al.* [1994] method for calculating distributed velocities. *Oki and Sud* [1998] and *Oki et al.* [1999] continued this line of application through the development of topographically corrected integrating pathways for routing models.

[6] More recent studies have attempted to include temporally variable estimates of flow velocity. *Schultze et al.* [2005] estimated velocity using the Manning-Strickler formula, in which velocity is a function of channel slope, channel roughness, and hydraulic radius of the river. Given the difficulty of estimating roughness and hydraulic radius over large areas, roughness was treated as a constant, or alternatively, a tuning parameter. Hydraulic radius was estimated on the basis of mean downstream discharge. *Ngo-Duc et al.* [2007] built on this approach to implement a variable-velocity routing scheme globally. In their application, roughness was calculated as a function of channel geometry and slope, and subgrid-scale meandering was accounted for in the calculation of velocity.

[7] Each of the routing studies described above utilized a "cell-to-cell" (CTC) algorithm, in which runoff flux from each analysis cell is routed to its downstream neighbor and is tracked along the river network on the basis of mass continuity equations [*Liston et al.*, 1994; *Miller et al.*, 1994]. Such CTC algorithms have been implemented with success over a range of spatial scales [e.g., *Bell et al.*, 2007; *Coe*, 1997]. They have the advantage of reporting routed discharge estimates at every point in the simulation domain, with the additional advantage that they can be coupled with land surface models (LSMs) to simulate feedbacks between laterally transferred moisture and other water and energy fluxes. CTC algorithms, however, do not consider within-cell routing, leading to considerable inaccuracies when grid-cell size is large relative to hydraulic heterogeneities. This is a particular concern because of the computationally intensive nature of CTC algorithms [*Olivera et al.*, 2000], which discourages high-resolution implementations for continental or global simulations even on today's powerful computers.

[8] An alternative to CTC routing is to employ some form of "source-to-sink" (STS) routing algorithm [e.g., *Lohmann et al.*, 1996; *Naden*, 1993; *Olivera and Maidment*, 1999; *Olivera et al.*, 2000]. In contrast to CTC algorithms, in which all runoff must be routed explicitly through the conveyance and storage equations of every cell between a runoff source and the discharge point of interest, STS solves for discharge only at selected points on the landscape. This approach allows for great efficiency, as the discharge at these selected points can be solved by applying a watershed response function to all sources of runoff within the drainage basin. Such efficiency is particularly useful for application to long analyses on the global scale, as one is often interested in discharge at only a small number of points—e.g., river outlets to the ocean or the locations of reliable river gauges—relative to the prohibitively large number of grid cells that would be included in a global-scale CTC algorithm implemented at high resolution. The high-resolution implementation of STS requires only that spatially variable static hydrographic parameters relevant to routing be defined at high resolution. This is done once during preprocessing and does not require any additional computational time during the routing simulation.

[9] Here we present results of a source-to-sink routing scheme developed for the Global Land Data Assimilation System (GLDAS [*Rodell et al.*, 2004]). GLDAS utilizes the Land Information System (LIS [*Kumar et al.*, 2006]) software to drive a suite of advanced land surface models with observation-based inputs toward the goal of optimal simulation of global land surface states and fluxes. GLDAS results have been used in the initialization of climate modeling experiments [e.g., *Koster et al.*, 2004], in the evaluation and interpretation of new satellite data records [e.g., *Syed et al.*, 2008], and in the study of land-atmosphere interactions [e.g., *Zhang et al.*, 2008]. Evaluation of GLDAS, however, has generally been limited to the United States and other observation-rich regions of the world [*Kato et al.*, 2007], even though one of its strengths is the provision of information on land surface processes in data poor regions. The need for a means of validating GLDAS was a primary motivation for the development of the routing scheme described here, as river gauge comparisons allow for some degree of model evaluation in regions (much of the world, in fact) where the observations necessary for a more thorough assessment of GLDAS model outputs are not available. Specifically, the scheme enables evaluation of the quantity, timing, and daily to interannual variability of simulated runoff. These, in turn, reflect the accuracy of model parameter fields and meteorological forcings, strengths and weaknesses of the parameterizations of various physical processes, and resolution and computational economics issues. Ultimately, we hope to use this information to guide model development and to identify optimal inputs and model configurations. Such applications must be pursued with the recognition that our present STS algorithm, as described in the next section, includes large lakes and reservoirs but does not account for water withdrawals or active reservoir

management. STS results for heavily managed rivers must therefore be interpreted with caution.

2. Source-to-Sink Algorithm

[10] The STS algorithm employed here is based on the algorithm presented by *Olivera et al.* [2000]. It is founded on the concept that the discharge hydrograph at a selected "sink" on the landscape can be described as the sum of watershed response functions for all "sources" of runoff within the drainage basin:

$$\mathbf{Q}_i = \sum_j \mathbf{Q}_j, \tag{1}$$

where $\mathbf{Q}_i$ ($L^3\ T^{-1}$) is the discharge hydrograph at sink i, and $\mathbf{Q}_j$ ($L^3\ T^{-1}$) is model grid cell j's contribution to the hydrograph. Both $\mathbf{Q}_i$ and $\mathbf{Q}_j$ are vectors with a length equal to the number of time steps included in the hydrograph. $\mathbf{Q}_j$ is, in turn, a function of the area of source cell j (A_j), the time series of simulated runoff at j (vector $\mathbf{R}_j$ (L)), and the response function relating source j to sink i ($\mathbf{u}_j$):

$$\mathbf{Q}_j = A_j \mathbf{R}_j * \mathbf{u}_j, \tag{2}$$

where the asterisk represents the convolution integral, and vector $\mathbf{u}_j$ (T^{-1}) has a length equal to the number of time steps included in the response function for runoff from grid cell j to contribute to discharge at sink i.

[11] A_j is equal to the resolution of the LSM and $\mathbf{R}_j$ is drawn from LSM output. Following on earlier work [*Mesa and Mifflin*, 1986; *Naden*, 1992; *Troch et al.*, 1994], the response function $\mathbf{u}_j$ is assumed to be a first-passage-time distribution:

$$u_j(t) = \frac{1}{2t\sqrt{\pi(t/t_j)/\Pi_j}} \exp\left\{-\frac{\left[1-(t/t_j)\right]^2}{4(t/t_j)/\Pi_j}\right\}. \tag{3}$$

This function includes two parameters that must be defined for each source cell: the average flow time to sink (t_j) and the representative Peclet number (Π_j), which describes the importance of advection relative to hydrodynamic dispersion over the path from source to sink. Both of these parameters, in turn, depend on estimates of flow length (L) and flow velocity (v) distributed over the flow path:

$$t_j = \sum_k \left(\frac{1}{v_k} L_k\right), \tag{4}$$

$$\Pi_j = \left[\sum_k \left(\frac{1}{v_k} L_k\right)\right]^2 \Bigg/ \left[\sum_k \left(\frac{D_k}{v_k^3}\right) L_k\right]. \tag{5}$$

In [4, 5], k refers to the segment of the flow path between j and i for which local velocity, flow length, and dispersivity (D ($L^2\ T^{-1}$)) are defined. It is important to note that the size of k can be much smaller than that of the model grid cell j. As routing parameters in STS are static, there is only a modest initial computational cost associated with the definition of high-resolution response functions; once these parameters are established, there is no additional computational expense for having defined the parameters at high resolution.

[12] For application to GLDAS, L_k and v_k were defined globally at 1 km resolution using the USGS EROS Hydro1k hydrologically corrected terrain data set [*Verdin and Verdin*, 1999]. Hydro1k is commonly used for global applications on account of its high resolution and general reliability; however, any discrepancies between Hydro1k basins or flow paths and the hydrography of the actual gauged basin will have an impact on our STS results. Weighted flow lengths were calculated using the hydrology functions available in ESRI ArcGIS 9.2, a set of spatial analysis tools that make it possible to describe hydrologic characteristics of a surface, including flow direction, watershed boundaries, and stream networks, on the basis of gridded elevation data. No correction was made for subgrid-scale sinuosity, as we assumed that the 1 km scale of calculation was sufficient to include meanders relevant to total flow time in these large river basins. This assumption is subject to re-examination in future applications of the STS algorithm. Velocity was estimated as a function of slope following the method of *Coe* [2000]:

$$v_k = v_0 (s_k/s_0)^{0.5}, \tag{6}$$

where v_0 is the minimum effective velocity of a river (0.8 m s^{-1}), s_k is local slope (m m^{-1}), and s_0 is a reference slope of 0.0005. This general approach to estimating velocity has been used in a number of previous studies [e.g., *Costa and Foley*, 1997; *Miller et al.*, 1994], with some variability in the choice of coefficients. Lakes and reservoirs were assigned a slower velocity, calculated as

$$v_k = v_L (A_k/A_L)^{0.5}, \tag{7}$$

where v_L is a reference minimum lake velocity (0.08 m s^{-1}), A_k is the area of the grid cell, and A_L is the total area of the lake. This formulation also derives from *Coe* [2000], with the modification that we do not account for lake depth in our calculation. Lakes were defined using the 5′ global surface water database produced by *Graham et al.* [1999]. This data set includes reservoirs, so the STS parameterization does account for the time-mean impact that these reservoirs have on river flow.

[13] Small or recently constructed reservoirs are not included in the present analysis, nor is active reservoir management. It would be possible to include these elements in the future, more detailed applications of STS. In the current application, the absence of small reservoirs and active reservoir management is expected to influence STS results in several ways. For intensely managed river basins (e.g., Columbia, Colorado), total transport time and evaporative loss during transport will both be underestimated, and in some cases, the simulated hydrograph may overestimate variability due to the absence of the moderating effect that reservoir management has on discharge. These discrepancies will be particularly significant when small reservoirs dominate the basin; in river basins characterized by large lakes and reservoirs, such as the St. Lawrence and Nelson, the storage impact of these large water bodies on the hydrograph will generally overwhelm that of smaller reservoirs and local management; large lakes and reservoirs are included in our calculation of STS parameters.

[14] As advection is known to dominate over hydrodynamic dispersion in large basins [*Olivera and Koka*, 2004],

the dispersivity coefficient D was set to a constant value of 900 m^2/s globally [after *Olivera et al.*, 2000]. Tests in which D was set to values as high as 2700 m^2/s and as low as 300 m^2/s confirmed the fact that results for the large basins considered in this study were relatively insensitive to this parameter.

[15] The timing and magnitude of the discharge hydrograph is also influenced by losses during transport. In *Olivera et al.* [2000], these losses were accounted for in a "loss coefficient" (λ) assigned to each grid cell. In this application we modified this approach, and estimated losses due to direct evaporation on the basis of potential evaporation, estimated river width, and local river velocity:

$$\mathrm{Evap}_j = W_j \cdot \sum_k \left(E_k \frac{1}{v_k} L_k \right), \tag{8}$$

where Evap_j (m) is the path-integrated evaporative loss for runoff originating in cell j, W_j is the river width attributable to runoff contributed from cell j, expressed as a fraction of total routing cell width, E_k is the potential evaporation at routing cell k, and v_k and L_k are local velocity and flow length, as defined previously.

[16] To calculate W_j, we first estimated river width at every cell in the landscape using the method of *Arora and Boer* [1999]:

$$\mathrm{Width}_k = \max\left(10, \left(6.0 + 10^{-4} \cdot Q_i\right) \cdot Q_k^{0.5}\right). \tag{9}$$

The local discharge Q_k (m^3/s) was calculated as the long-term average simulated runoff, integrated for all points upstream of k, without accounting for evaporation. Discharge at outlet (or gauge location) Q_i was calculated the same way. For basins in which gauged discharge at i significantly differed from simulated discharge, both Q_i and Q_k were linearly corrected by multiplying by the ratio of gauged to simulated discharge. Width at gauge location, Width_i (m), was extracted from the Width_k field, and W_j was estimated as

$$W_j = \mathrm{Width}_i \cdot \frac{Q_j}{Q_i} \frac{1}{\mathrm{CellWidth}}. \tag{10}$$

Local potential evaporation E_k (m/s) was calculated for each season (DJF, MAM, JJA, SON) as the Penman Potential Evaporation for an open water surface [*Monteith*, 1981; *Penman*, 1948], with all required meteorological data drawn from the GLDAS meteorological forcing files and surface conditions and parameters drawn from GLDAS output. When solving equation (8), the integration function takes into account seasonal changes in E_k for cells with a flow time that exceeds the remainder of the season in which runoff was generated.

3. Data and Implementation

3.1. Gauge Data

[17] Notwithstanding the recent decline in the number of active river gauges [*Vorosmarty*, 2001], river discharge continues to be one of the most widely and accurately measured elements of the hydrological cycle. Active or historical gauge data are available for many of the world's major rivers through the GRDC (http://grdc.bafg.de), a public data repository that receives gauge records from the national meteorological and hydrological services of World Meteorological Organization, Geneva (WMO), member nations. The GRDC archive currently includes data for 7332 gauges distributed around the world, though only a subset of these has been active in recent years. For this study, the GRDC provided daily discharge data from 66 of the world's largest rivers that had sufficient observations for the evaluation of GLDAS (Figure 1).

3.2. GLDAS

[18] The Global Land Data Assimilation System [*Rodell et al.*, 2004] is designed to provide optimal estimates of land surface fluxes and storages of water and energy. Satellite and ground-based observations are used to parameterize, drive, and constrain global offline simulations of advanced land surface models (LSMs), including Noah [*Chen et al.*, 1996; *Ek et al.*, 2003; *Koren et al.*, 1999], the Common Land Model (CLM [*Dai et al.*, 2003]), the Variable Infiltration Capacity (VIC) model [*Liang et al.*, 1994], and Mosaic [*Koster and Suarez*, 1996]. The GLDAS archive (http://disc.gsfc.nasa.gov/hydrology/index.shtml) contains output of these simulations at 1° and 1/4° (for Noah) resolutions beginning in 1979. GLDAS meteorological forcing data come from the Global Data Assimilation System (GDAS [*Derber et al.*, 1991]), supplemented with a downscaled version of the NOAA Climate Prediction Center's Merged Analysis of Precipitation (CMAP [*Xie and Arkin*, 1997]) and satellite-derived downward radiation from the Air Force Weather Agency [*Kopp and Kiess*, 1996]. Details of these forcing data are provided in *Rodell et al.* [2004] and *Kato et al.* [2007]. Recently, the GLDAS record has been extended back in time, with 52 year simulations carried out at 1° for the period 1948-2000 using atmospheric forcing data from the "Global Meteorological Forcing Dataset for land surface models" described by *Sheffield et al.* [2006].

[19] In this paper the STS algorithm is applied to 27 years of multimodel GLDAS output (October 1979–October 2007) for four LSMs: Noah version 2.7, CLM version 2.0, VIC version 4.0.4 (with some patches from 4.0.5) run in water balance mode, and Mosaic. The influence of forcing data is also considered by including STS analyses of the 52 year 1° GLDAS-Noah simulation (October 1948–October 2000). Initial surface states in all GLDAS simulations are drawn from climatological time-of-year averages for long simulations with the relevant LSM [*Rodell et al.*, 2005]. Details on the five GLDAS simulations included in this study are provided in Table 1.

3.3. Land Surface Models

3.3.1. Noah

[20] The Noah LSM [*Chen et al.*, 1996; *Ek et al.*, 2003; *Koren et al.*, 1999] was developed through a collaboration of public and private institutions under the leadership of the National Centers for Environmental Prediction (NCEP). It is a one-dimensional, free-standing column model that can be run in uncoupled mode or can be coupled with atmospheric models. Noah simulates skin temperature, soil temperature and moisture (liquid and frozen) for all soil layers (four in this application), snow depth, snow water equivalent, canopy water content, and surface energy and water fluxes. It has been used operationally in NCEP models for over a

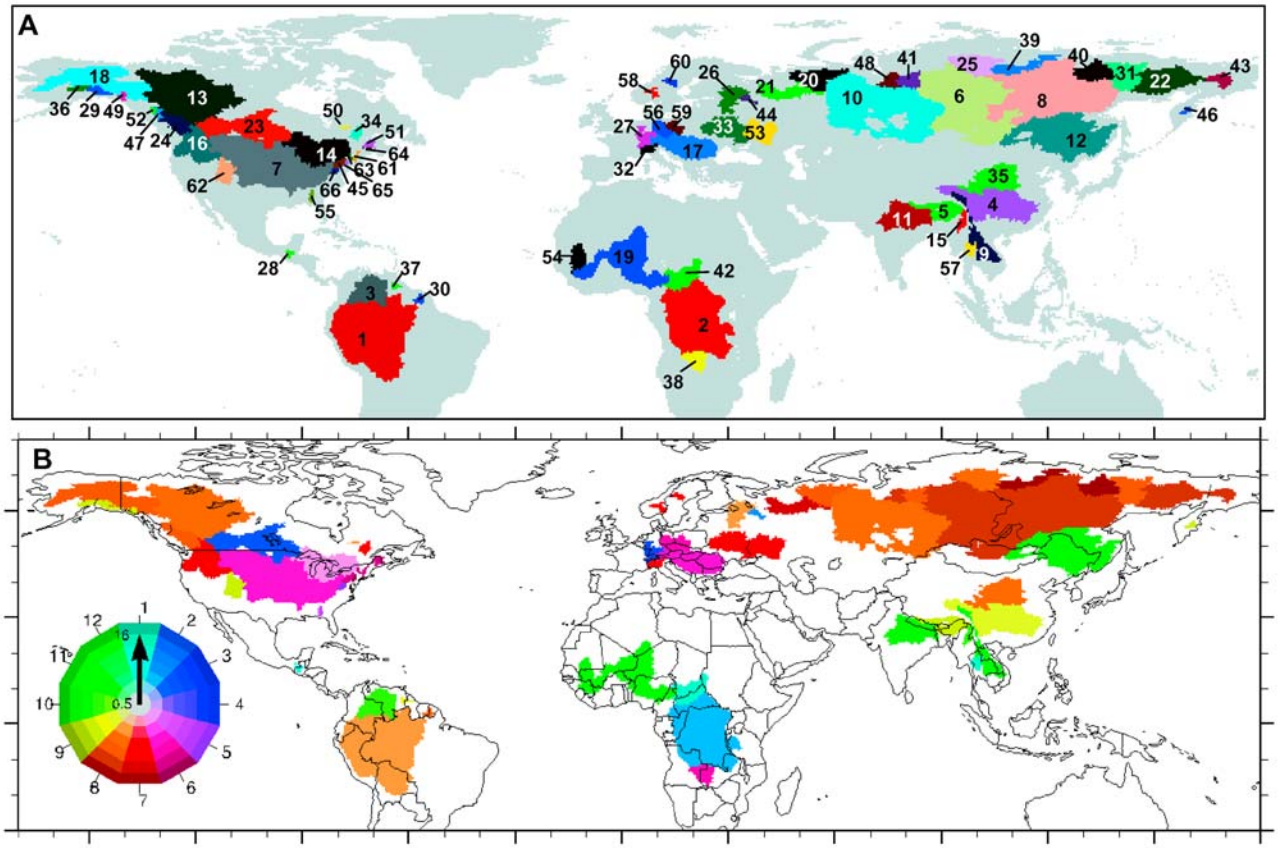

	River	Station	Lat	Lon	Area		River	Station	Lat	Lon	Area
1.	Amazon	Obidos	-1.9	-55.5	4,640,300	34.	Saguenay	Centrale d'Isle Maligne	48.6	-71.6	73,000
2.	Congo	Kinshasa	-4.3	15.3	3,475,000	35.	Yellow	Huayuankuo	34.9	113.7	730,036
3.	Orinoco	Puenta Angostura	8.2	-63.6	836,000	36.	Susitna	Susitna Station	61.5	-150.5	50,246
4.	Yangtze	Datong	30.8	117.6	1,705,383	37.	Cuyuni	Kamaria Falls	6.4	-58.8	53,400
5.	Brahmaputra	Bahadurabad	25.2	89.7	636,130	38.	Zambezi	Katima Mulilo	-17.5	24.3	334,000
6.	Yenisey	Igarka	67.5	86.5	2,440,000	39.	Olenek	7.5 km d/s of River Pur	72.1	123.2	198,000
7.	Mississippi	Vicksburg, MS	32.3	-90.9	2,964,255	40.	Yana	Ubilieynaya	70.8	136.1	224,000
8.	Lena	Kyusyur	70.7	127.7	2,430,000	41.	Taz	Sidorovsk	66.6	82.3	100,000
9.	Mekong	Stung Treng	13.5	105.9	635,000	42.	Chari	Ndjamena	12.1	15.0	600,000
10.	Ob	Salekhard	66.6	66.5	2,949,998	43.	Anadyr	Snezhnoye	65.5	173.0	106,000
11.	Ganges	Hardinge Bridge	24.1	89.0	846,300	44.	Volga	Rybinskaya Ges	58.2	38.7	150,000
12.	Amur	Bogorodsokoye	52.5	140.5	1,790,000	45.	Susquehann	Harrisburg, PA	40.3	-76.9	62,419
13.	Mackenzie	Arctic Red River	67.5	-133.7	1,660,000	46.	Kamchatka	Bolshie Scheki	56.3	161.7	51,600
14.	St. Lawrence	Lasalle	45.4	-73.6	944,421	47.	Skeena	Usk	54.6	-128.4	42,200
15.	Irrawaddy	Sagaing	22.0	96.1	117,900	48.	Pur	Samburg	67.0	78.2	95,100
16.	Columbia	Beaver Army Terminal	46.2	-123.2	665,371	49.	Alsek	Near Yakutat Alas	59.4	-138.1	28,024
17.	Danube	Caetal Izmail	45.2	28.7	807,000	50.	Rupert	En Aval du Lac Nemiscau	51.4	-76.9	40,900
18.	Yukon	Pilot Station	61.9	-162.9	831,390	51.	St. John	Below Macraquac	46.0	-66.8	39,900
19.	Niger	Lokoja	7.8	6.8	2,078,465	52.	Nass	Above Shumal Creek	55.3	-129.1	19,200
20.	Pechora	Oksino	67.6	52.2	312,000	53.	Don	Razdorskaya	47.5	40.6	378,000
21.	Severnaya Dvina	Ust-Pinege	64.2	41.9	348,000	54.	Senegal	Bakel	14.9	-12.5	218,000
22.	Kolyma	Emtegei	62.8	146.5	533,032	55.	Apalachicol	Near Sumatra, FL	29.9	-85.0	49,728
23.	Nelson	Long Spruce Gen. Stn.	56.4	-94.4	1,060,000	56.	Elbe	Neu-Darchau	53.2	10.9	131,950
24.	Fraser	Hope	49.4	-121.5	217,000	57.	Chao Phray	Khai Chira Prawat	15.7	100.7	110,569
25.	Khatanga	Khatanga	72.0	102.5	275,000	58.	Glama	Solbergfoss	59.6	11.2	40,540
26.	Neva	Novosaratovka	59.8	30.5	281,000	59.	Oder	Hohensaaten-Finow Ap	52.9	14.1	109,564
27.	Rhine	Rees	51.8	6.4	159,300	60.	Angermana	Sollefteae Krv	63.2	17.3	30,638
28.	Usumacinta	Boca del Cerro	17.4	-91.5	47,697	61.	Connecticut	Thompsonville, CT	42.0	-72.6	25,019
29.	Copper	Million Dollar Bridge	60.7	-144.7	62,678	62.	Colorado	Lee's Ferry, AZ	36.9	-111.6	289,562
30.	Maroni	Langa Tabiki	5.0	-54.4	60,930	63.	Hudson	Green Island, NY	42.8	-73.7	20,953
31.	Indigirka	Vorontsovo	69.6	147.4	305,000	64.	Penobscot	Eddington, ME	44.8	-68.7	19,464
32.	Po	Pontelagoscuro	44.9	11.6	70,091	65.	Potomac	Near Washington DC	38.9	-77.1	29,940
33.	Dnepr	Dnepr Power Plant	47.9	35.2	463,000	66.	Delaware	Trenton, NJ	40.2	-74.8	17,560

Figure 1. (a) Basins included in the study. (b) Evans plot showing the month of peak discharge (color hue) and magnitude of the annual range in discharge (maximum daily flow-minimum daily flow) as a fraction of to mean discharge (color saturation), based on Global Runoff Data Center (GRDC) gauge climatologically averaged daily data.

Table 1. Simulations Included in the Study[a]

Name	LSM	Time Period	Forcing Reference
N1	Noah 2.7	1979–2007	GDAS+CMAP+AGRMET
C1	CLM 2.0	1979–2007	GDAS+CMAP+AGRMET
V1	VIC 4.0.4	1979–2007	GDAS+CMAP+AGRMET
M1	Mosaic	1979–2007	GDAS+CMAP+AGRMET
N50+	Noah 2.7	1948–2000	*Sheffield et al.* [2006]

[a]Forcing data sets are described in the text. VIC 4.0.4 is run in water balance mode.

decade, and is in active development. Noah applies finite difference spatial discretization methods and a Crank-Nicholson time-integration scheme to solve the governing physically based equations of the soil-vegetation-snowpack medium. Of relevance to this study, Noah 2.7 includes treatment of frozen soil physics, but has a relatively simple, one-layer snow model. This version of the model is known to suffer from an early melt bias [*Sheffield et al.*, 2003; *Zaitchik and Rodell*, 2009] that has been addressed in subsequent model development.

3.3.2. Common Land Model (CLM)

[21] CLM [*Dai et al.*, 2003] is a community supported model built on components of the NCAR land surface model [*Bonan*, 1998], the biosphere-atmosphere transfer scheme [*Dickinson et al.*, 1993], and the LSM of the Institute of Atmospheric Physics of the Chinese Academy of Sciences [*Dai and Zeng*, 1997]. Like Noah, CLM is a stand-alone one-dimensional model that can run in uncoupled or coupled mode. Numerically, the model uses finite difference spatial discretization methods and a fully implicit time-integration scheme to integrate governing equations. CLM 2.0, the version used in this study, divides the soil column into ten horizontal layers. Notably, CLM 2.0 has a smaller dynamic soil moisture range than other models included in the study, which leads to higher simulated runoff (and lower simulated evapotranspiration) under wet conditions. CLM includes a multiple layer snow model and accounts for frozen soil physics.

3.3.3. Variable Infiltration Capacity (VIC) model

[22] Unlike the other GLDAS LSMs included in this study, the VIC model [*Cherkauer and Lettenmaier*, 1999; *Liang et al.*, 1994, 1996] was developed as an uncoupled, calibrated hydrology model, and was only later adopted for coupling with climate models [*Mitchell et al.*, 2004]. VIC 4.0.4 is a one-dimensional, stand-alone LSM that can be run in either an energy balance or a water balance mode. It is important to note that within GLDAS, VIC is currently only run in water balance mode, meaning it does not solve the surface energy balance explicitly and does not include frozen soil physics. VIC 4.0.4 contains three soil layers and a two layer snow model. The energy balance within the snowpack is solved even when VIC is run in water balance mode. VIC also has the capability to define subgrid snow bands on the basis of elevation, but this feature was not activated. VIC has been applied in numerous studies of large river basins [*Lohmann et al.*, 1998; *Nijssen et al.*, 1997] and at the continental and global scales [*Maurer et al.*, 2002; *Nijssen et al.*, 2003].

3.3.4. Mosaic

[23] Mosaic [*Koster and Suarez*, 1996] is a stand-alone, one-dimensional LSM that was originally developed for use with the NASA global climate model. The Mosaic physics and surface flux calculations are based on those of the simple biosphere model [*Sellers et al.*, 1986]. The model includes three soil layers and a simple one-layer snow model in which melt rate is calculated as the residual of the surface energy balance. Mosaic was the first LSM that allowed grid cells to be subdivided into vegetation tiles to allow for the simulation of subgrid-scale variability [*Avissar and Pielke*, 1989]. GLDAS applies Mosaic's tiling approach to all LSMs, including Noah, CLM, and VIC, in order to represent subgrid vegetation heterogeneity in relatively coarse simulations (1° in this application). Multiple vegetation types and/or bare ground defined by the 1 km UMD land cover data set [*Hansen et al.*, 2000] can coexist within a grid if they cover more than 10% of total tiles. The grid fluxes and states are weighted average of tiles.

3.4. Implementation of STS

[24] The STS algorithm was applied to GLDAS gridded runoff fields as a post-processor. The convolution integral was solved using a fast-Fourier transform (FFT) applied to daily surface and subsurface GLDAS runoff. The FFT was used to calculate instantaneous hydrographs on an annual basis, allowing for a response function $\mathbf{u}_j$ of length = 900 days, which is long enough to capture the dispersion tail of the longest estimated flow times. Annual hydrographs were summed to produce a continuous record that includes the long tail of the response function. The first 2 years of calculated discharge were discarded in the analyses of results to remove initial condition effects.

[25] In the calculation of travel time t_j, 15 days were added for subsurface runoff, as an estimate for in-cell delays during infiltration and lateral flow, while only 2 h were added to surface runoff [*Coe*, 2000; *Costa and Foley*, 1997]. These are first-order approximations based on earlier modeling experience and will need to be refined in future analyses. The influence of these parameters on STS output is greater for smaller basins, in which in-cell transport represents a larger fraction of total flow time. Nearest-neighbor sampling was used to assign GLDAS grid cells to STS drainage basins. For the purposes of this methodological study, STS "sinks" were the gauge locations for all major basins for which adequate river gauge data were available from the GRDC. These basins provide extensive coverage of global land areas, including the full range of climate and ecological zones (Figure 1). Global STS parameter fields have also been generated, and are available upon request from the authors.

4. Results

[26] Three elements of the GLDAS-STS simulated hydrographs are considered: (1) mean discharge, (2) seasonal and intraseasonal variability, and (3) interannual variability. In each case, results are presented for multiple models implemented using the standard GLDAS forcing, simulations N1, C1, V1, and M1, as defined in Table 1, as well as for a single model, Noah, implemented with the *Sheffield et al.* [2006] atmospheric forcing data set (N50+). In presenting our results, we compare simulations to gauged discharge for all dates on which gauged data are available for each basin. For this reason, the evaluation period is different for basins with limited gauge records. Similarly, the gauge comparison

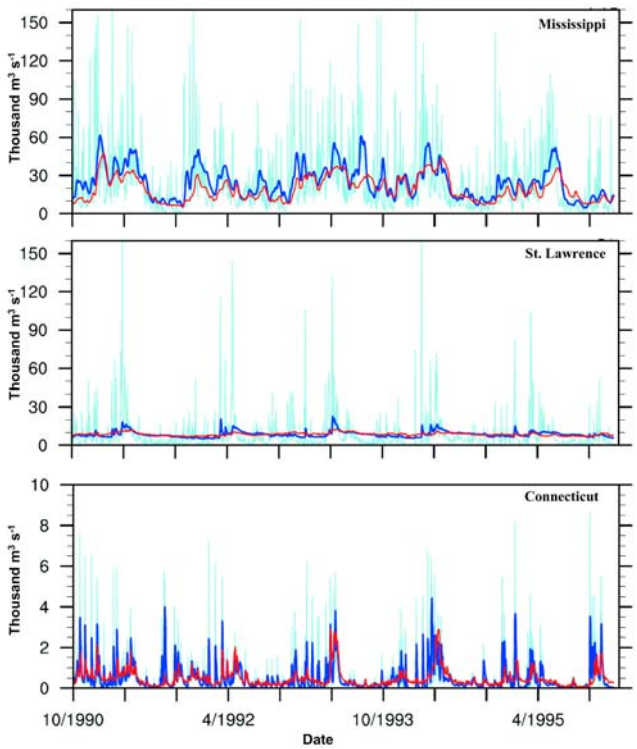

Figure 2. Hydrograph of daily average rates of: summed C1 distributed surface and subsurface runoff (light blue), C1 STS-routed simulated discharge (dark blue), and GRDC observed discharge (red) for the Mississippi, St. Lawrence, and Connecticut rivers. Units are thousand meters cubed per second.

data record for N50+ differs from that of other simulations due to the difference in time coverage.

[27] In general, STS routing produced simulated discharge hydrographs that were smoothed and had a delayed peak relative to the time series of simulated GLDAS runoff for the watershed (e.g., Figure 2), as a routing scheme should. As expected, smoothing and delay were most pronounced for large watersheds and for those with more lake coverage.

4.1. Annual Discharge

[28] Figure 3 lists mean flow rate for each simulation in selected rivers, along with the corresponding gauged average. The contribution of the routing scheme to this result is relatively minor, as evaporative loss during transport is small relative to mean discharge in almost all cases (<5% of mean simulated runoff in all basins, for all models). Use of the STS routing scheme does, however, facilitate the comparison with gauged discharge in cases where gauge reports are sporadic; without a routing scheme, there is no way to determine proper dates of comparison for an incomplete gauge data set.

[29] For standard GLDAS forcing, the four LSMs differed substantially in their simulation of mean discharge over the observed record (Figure 4). C1 exhibited the largest average discharge, producing estimates that were generally higher than observed discharge for much of Europe, all basins in Africa, and certain basins in North America and Asia. N1 results were somewhat drier: simulated discharge was lower than observed for all large basins in the Western Hemisphere and for several in Asia. Results in Europe and Africa were, on average, somewhat wetter than observed. V1 discharge estimates were lower than observed for almost all basins, with the largest discrepancies occurring in North and South America and in Asia. M1 results were similar to V1. Summed for each continent, and defining estimation within 20% of observed discharge as accurate, V1 and M1 underestimated total discharge for Africa, South America, North America, and Asia, N1 was low in South America, North America, and Asia, C1 underestimated only for South America, and N50+ was not systematically low for any continent (Figure 5). C1 and N50+ produced high discharge estimates relative to observations in Europe and Africa. Summed over all continents, the C1 and N50+ simulations were within 20% of gauged discharge while all other simulations were dry relative to observation.

[30] Low estimates of discharge in the M1 simulation are generally consistent with earlier studies in which Mosaic has often yielded above-average evapotranspiration and soil moisture variability and low estimates of runoff relative to other LSMs [*Kato et al.*, 2007; *Lohmann et al.*, 2004]. The low discharge values of V1 differ from some other multi-model comparison studies, possibly because we used VIC in water balance mode. In studies that have applied VIC in full energy balance mode, the model has been known to yield high estimates of runoff and low estimates of evapotranspiration relative to Mosaic and other LSMs [e.g., *Lohmann et al.*, 2004; *Slater et al.*, 2007]. Efforts are underway to implement a full energy balance version of VIC within GLDAS.

[31] We note that the low runoff tendency of GLDAS in most basins cannot be attributed to the STS routing scheme. Evaporative losses during transport were small relative to the difference between gauged discharge and simulated runoff in all cases, and routing simulations in which evaporative loss was set to 0 yielded results of the same character. As the routing scheme only accounts for direct evaporation from the river channel, it produces conservative estimates of loss during transport, particularly for basins that include inland deltas, human water withdrawals, or significant re-infiltration from the river bed. For this reason, simulations with discharge estimates higher than observation may be somewhat more accurate than those that yield low estimates of discharge.

[32] Results of the N50+ simulation demonstrate the importance of the meteorological forcing data set. Where the N1 simulation produced underestimates of discharge throughout North and South America, N50+ returned mixed results on those continents (Figure 4e). Indeed, in the global average N50+ simulation yielded the smallest bias relative to observed discharge of any simulation. This result does not, in itself, allow for a definitive judgment on the two forcing data sets because how a model partitions precipitation into runoff and evapotranspiration is as important as the precipitation input itself. What can be said is that for typically configured simulations implemented at 1° resolution, the standard GLDAS atmospheric forcing causes Noah, VIC, and Mosaic to underestimate runoff. The *Sheffield et al.* [2006] data set causes Noah to produce more runoff, and thus to be more consistent with observed discharge data.

[33] It is noteworthy, however, that the GLDAS forcing led to underestimation of runoff for three out of four LSMs.

	Mean Discharge (m3/s)							Peak Day (Day of Hydrologic Year)						
River	GRDC	N1	C1	V1	M1	GRDC50	N50+	GRDC	N1	C1	V1	M1	GRDC50	N50+
Amazon	169,375	99,619	107,707	67,884	67,001	172,763	153,381	242	72	242	253	270	246	270
Congo	37,966	33,478	40,070	12,644	5,893	42,152	57,436	71	221	220	220	220	70	52
Yenisey	19,204	9,704	17,876	8,826	9,098	18,835	12,405	249	229	240	258	264	249	222
Mississippi	18,554	12,377	24,569	10,588	8,309	17,299	30,804	170	200	161	194	225	194	213
Mekong	13,408	8,496	9,967	5,816	2,746	13,319	10,631	343	340	339	339	374	342	357
Ganges	11,091	7,220	10,571	2,983	1,790	11,091	16,797	333	333	307	331	316	332	346
Mackenzie	8,474	3,787	8,458	2,219	2,373	8,552	8,014	235	214	235	252	271	258	199
Yukon	6,518	5,357	7,772	4,134	5,134	6,366	3,123	246	238	255	273	293	245	223
Kolyma	3,143	3,133	4,156	1,636	2,538	3,279	3,384	254	241	241	264	272	253	228
Rhine	2,446	2,698	3,201	2,313	2,426	2,327	4,055	100	100	83	179	227	136	232
Copper	1,760	3,361	3,624	3,532	3,619	1,760	1,537	280	241	265	240	265	279	245
Po	1,530	1,034	1,429	857	761	1,539	2,226	238	244	239	182	239	242	208
Glama	703	574	673	517	573	687	671	244	251	220	229	264	243	252
Connecticut	505	388	483	442	356	482	498	190	186	182	183	200	188	200
Colorado	424	87	467	38	74	391	562	275	233	228	299	222	255	280

	Daily Standard Deviation							Annual range (m3/s)						
River	GRDC	N1	C1	V1	M1	GRDC50	N50+	GRDC	N1	C1	V1	M1	GRDC50	N50+
Amazon	48,637	48,213	42,866	36,719	29,956	49,670	46,208	132,037	116,225	108,349	86,057	63,527	130,638	111,155
Congo	9,111	19,204	21,249	7,150	4,842	10,032	19,139	30,262	67,682	122,204	27,364	37,383	27,812	55,942
Yenisey	23,131	12,454	29,025	11,445	13,225	24,962	9,766	94,141	33,285	114,324	36,794	42,778	94,769	37,280
Mississippi	9,421	10,254	14,437	8,955	6,214	9,728	15,745	19,008	21,294	27,076	21,529	13,061	19,426	36,614
Mekong	13,998	12,005	12,257	8,690	3,661	13,816	11,528	42,880	37,790	38,274	27,822	9,963	37,889	32,258
Ganges	15,452	11,797	16,991	4,127	2,061	15,452	22,580	42,561	34,969	51,555	11,052	5,702	42,561	64,020
Mackenzie	5,664	2,526	7,164	1,512	2,082	5,853	3,319	15,339	8,805	26,713	3,926	6,412	15,020	13,784
Yukon	5,693	6,024	11,060	4,515	7,298	5,502	2,816	16,411	17,947	32,560	11,679	19,129	15,487	9,379
Kolyma	5,239	6,156	10,682	1,934	4,722	5,239	5,514	15,256	26,232	46,033	7,261	17,887	16,246	20,396
Rhine	1,286	2,196	2,356	1,947	1,957	1,188	1,778	2,062	4,142	4,348	3,723	4,418	1,477	3,632
Copper	1,967	3,792	4,309	5,275	4,705	1,967	1,600	5,115	11,217	12,178	16,201	13,528	5,115	4,891
Po	943	825	1,155	806	670	943	1,157	2,686	1,955	2,798	2,291	1,704	2,420	2,576
Glama	424	464	848	559	615	436	430	1,071	1,040	2,599	1,434	1,710	1,134	1,239
Connecticut	465	386	653	657	451	467	438	1,249	697	1,244	1,259	1,347	1,306	1,295
Colorado	214	74	351	38	54	325	288	235	68	507	39	50	527	466

	Daily Correlation (m3/s)							Interannual Standard Deviation (m3/s)						
River	GRDC	N1	C1	V1	M1	GRDC50	N50+	GRDC	N1	C1	V1	M1	GRDC50	N50+
Amazon	--	0.72	0.80	0.65	0.47	--	0.61	28,022	18,377	16,659	16,830	13,602	29,331	22,225
Congo	--	0.06	-0.02	-0.03	-0.06	--	0.69	4,190	18,760	30,193	7,418	7,284	5,320	10,167
Yenisey	--	0.29	0.62	0.74	0.62	--	0.21	5,246	3,967	5,532	5,559	3,602	3,541	4,407
Mississippi	--	0.83	0.78	0.78	0.62	--	0.80	3,023	4,371	7,353	4,137	3,410	3,397	6,779
Mekong	--	0.90	0.91	0.81	0.52	--	0.85	3,076	1,287	1,901	1,665	1,132	2,865	1,971
Ganges	--	0.93	0.89	0.78	0.85	--	0.87	4,462	2,461	4,516	1,301	647	4,462	5,750
Mackenzie	--	0.42	0.55	0.51	0.77	--	0.11	1,812	1,149	2,771	1,153	730	1,943	3,469
Yukon	--	0.61	0.73	0.61	0.61	--	0.30	1,778	2,777	3,296	2,607	3,029	1,605	1,128
Kolyma	--	0.49	0.34	0.74	0.74	--	0.42	1,269	1,277	1,458	1,377	1,345	1,341	968
Rhine	--	0.65	0.70	0.66	0.46	--	0.50	670	980	919	943	950	760	776
Copper	--	0.63	0.45	0.40	0.82	--	0.66	387	643	1,328	872	870	387	332
Po	--	0.47	0.71	0.54	0.41	--	0.48	559	522	515	398	297	565	730
Glama	--	0.32	0.37	0.28	0.50	--	0.52	195	207	213	235	201	177	136
Connecticut	--	0.63	0.70	0.64	0.57	--	0.66	162	185	188	206	166	136	143
Colorado	--	0.55	0.39	0.53	0.35	--	0.41	259	60	253	26	47	283	207

Figure 3. Mean annual discharge, climatological peak discharge day, standard deviation of daily discharge, climatological average range between annual high flow and low flow, correlation of daily discharge with GRDC gauge data, and interannual standard deviation in peak flow volume for rivers representing a range of climate conditions, geographies, and basin sizes. For mean discharge, daily standard deviation, annual range, and standard deviation of annual peak flow rate, blue shading indicates simulation values that are 20% larger than observed or more, orange indicates values that are 20% lower than observed or less, and green indicates values within 20%. For peak day, blue indicates simulated peaks that are 20 or more days earlier than observed, orange peaks that are 20 or more days later, and green peaks that are within 20 days of the observation. Values of peak day are for the day of the hydrologic year (1 October–30 September). For daily correlations, correlation values greater than 0.7 are shaded green and less than 0.3 are shaded orange. Note that the period of gauge evaluation for N50+ (GRDC50) differs from that of other simulations.

The GLDAS precipitation data set was selected as a result of extensive comparison between available precipitation forcing options [*Gottschalck et al.*, 2005]. Nevertheless, its precipitation forcing (derived from CMAP) has a low bias relative to a number of earlier precipitation data sets that were used during the development of LSMs, and which likely informed parameterization of the models used in this study.

4.2. Timing of Peak Flow

[34] In analyzing the simulation of seasonal discharge variability, we consider both timing and magnitude of peak flow. The day of annual maximum flow is a useful indicator of whether the GLDAS-STS system properly captures the seasonal cycle of runoff. Differences between simulations reveal key strengths and possible weaknesses of each model

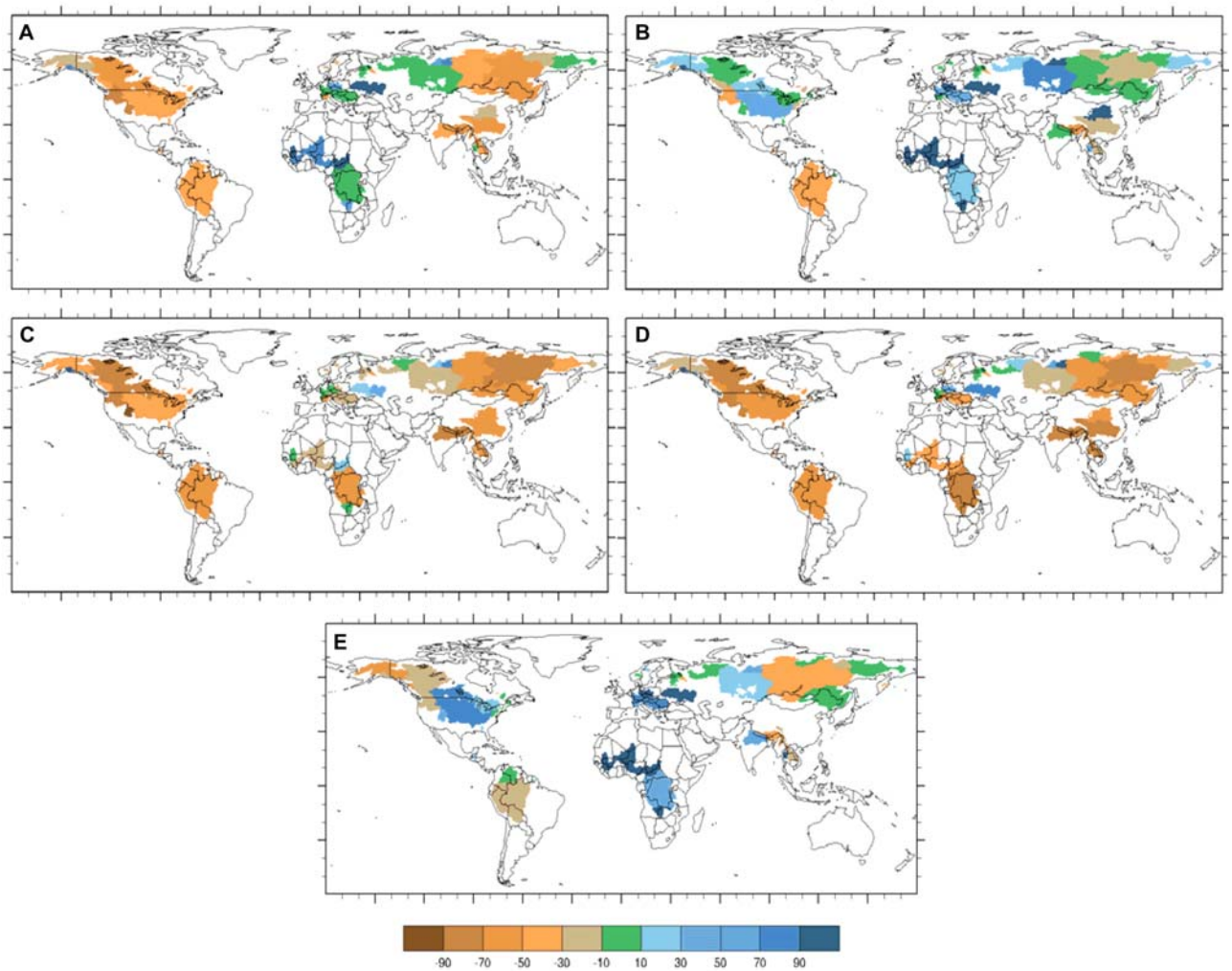

Figure 4. Mean annual simulated discharge for each of the five simulations included in the study, mapped as the percentage difference from GRDC reported discharge: 100 * Simulated/Observed through 100. Brown colors indicate simulations that are dry relative to observation, blues indicate simulations that are wet relative to observation, and green indicates a simulation within 10% of observation.

within the GLDAS system. For example, in high-latitude basins, simulated peak discharge was systematically early in both the N1 and N50+ simulations (Figure 6). This is consistent with a known tendency of Noah v2.7: that it often exhibits premature melt in simulations of regions with a deep seasonal snowpack [e.g., *Sheffield et al.*, 2003; *Zaitchik and Rodell*, 2009], a bias that is associated with the model's low values for snow surface albedo. Recent experimental updates to the Noah model have sought to address this issue. The M1 simulation, meanwhile, exhibits systematically late discharge peaks in these same snow-dominated basins, suggesting that Mosaic retains the snowpack too late into the spring. Indeed, in applications to the United States, *Rodell and Houser* [2004] found that Mosaic had a tendency to overestimate snow cover in late winter and spring.

[35] Both V1 and C1 match the timing of observed discharge reasonably well in basins with deep snow, and these two simulations provide the best simulation of peak discharge timing globally as well. For V1, this is a testament to the model's legacy in hydrological applications. We note that the large difference between N50+ and the GLDAS evaluations in the Nelson River (central Canada) results from differences in the gauge evaluation data, not in the simulations themselves. In fact, all simulated hydrographs and gauge data indicate that the climatologically averaged seasonal hydrograph is essentially flat for this lake-dominated basin. Seemingly large differences in peak day result from small shifts in gauged discharge, and they should not be overinterpreted. The GLDAS simulations performed poorly in the Congo and Amur (Russia/China) basins, both of which have bimodal hydrographs. N50+, however, evaluated well in these basins. Poor GLDAS results are likely a product of errors in the precipitation forcing, combined with a short gauge record for evaluation. Finally, Figure 6f shows that a multimodel average generally matches the timing of gauge hydrographs better than any single GLDAS simulation. This is consistent with a guiding principle of GLDAS: that LSMs all have strengths and weaknesses, so a suite of models often provides better insight on land surface processes than does any single model [*Rodell et al.*, 2004].

	Mean Discharge (m3/s)						
	GRDC	N1	C1	V1	M1	GRDC50	N50+
NA	69,336	42,230	72,056	36,972	32,927	68,353	77,841
SA	204,821	118,362	129,724	80,805	79,508	207,302	189,950
EU	28,720	32,138	42,085	24,952	28,785	27,646	43,507
AS	164,318	91,919	148,455	64,997	64,565	136,415	113,567
AF	44,971	48,452	59,853	18,576	10,117	49,419	81,185
Total	512,166	333,101	452,173	226,302	215,902	489,134	506,049
	Peak Day (Day of Hydrologic Year)						
	GRDC	N1	C1	V1	M1	GRDC50	N50+
NA	213	206	200	214	245	214	201
SA	256	106	244	257	276	259	276
EU	200	197	201	218	235	207	232
AS	289	269	257	272	283	283	265
AF	114	252	247	254	246	110	135
	Daily Standard Deviation (m3/s)						
	GRDC	N1	C1	V1	M1	GRDC50	N50+
NA	4,502	4,830	7,962	4,333	3,895	4,528	7,590
SA	43,743	42,937	38,375	32,684	26,577	44,718	42,361
EU	2,370	2,780	4,271	2,875	3,121	2,262	2,615
AS	14,263	10,022	20,938	7,387	7,681	15,026	12,102
AF	8,277	15,373	16,904	6,030	3,769	9,115	15,686
Total	73,155	75,942	88,450	53,310	45,043	75,649	80,354
	Annual range (m3/s)						
	GRDC	N1	C1	V1	M1	GRDC50	N50+
NA	101,841	91,204	161,360	95,543	84,125	102,243	112,971
SA	199,058	165,620	164,107	125,295	88,158	197,071	196,136
EU	57,421	56,043	109,346	61,719	72,406	51,823	53,009
AS	539,564	426,002	878,249	255,344	275,261	495,949	441,237
AF	50,381	119,273	193,633	50,568	49,466	49,378	116,142
Total	948,265	858,143	1,506,694	588,469	569,415	896,464	919,495
	Daily Correlation						
	GRDC	N1	C1	V1	M1	GRDC50	N50+
NA	--	0.57	0.61	0.59	0.58	--	0.60
SA	--	0.71	0.75	0.64	0.51	--	0.67
EU	--	0.48	0.56	0.52	0.46	--	0.55
AS	--	0.60	0.58	0.62	0.69	--	0.54
AF	--	0.24	0.09	0.16	0.13	--	0.72
	Interannual Peak Flow Variability (m3/s)						
	GRDC	N1	C1	V1	M1	GRDC50	N50+
NA	15,676	16,081	23,427	16,541	13,719	15,797	19,592
SA	34,312	25,458	22,750	22,056	18,868	33,959	28,681
EU	8,045	13,240	14,169	12,363	11,555	7,975	9,998
AS	41,137	33,986	55,051	35,201	28,423	30,565	30,236
AF	6,687	28,035	44,350	12,267	14,063	7,885	17,882
Total	105,856	116,800	159,747	98,427	86,627	96,181	106,389

Figure 5. As in Figure 3, but for continental, and where appropriate, global totals for the GRDC gauged basins included in this study. NA, North America; SA, South America; EU, Europe; AS, Asia; AF, Africa.

[36] Timing errors tended to balance out in the continental average (Figure 5), with some exceptions. Africa appears to be one such exception, though this is largely due to a paucity of evaluation data for the Congo River during the GLDAS period. GRDC gauge data for the Congo ends in 1984, providing only a short period of overlap with GLDAS. During this brief period, apparent errors in the precipitation forcing caused the N1, C1, V1, and M1 simulations to reverse the magnitude of the winter and summer discharge peaks of the bimodal Congo hydrograph (e.g., Figure 7a). In fact, over the entire 1979–2007 period, the GLDAS-STS simulations generally simulated the magnitude of these peaks correctly, placing the larger peak in winter (e.g., Figure 7b). The N50+ simulation also simulated these peaks correctly, and because a longer gauge record was available for that simulation, this fact is reflected in the results; N50+ discharge is high relative to gauge data, but the timing of peaks is approximately correct (Figure 7c). All simulations of the Congo would benefit from more detailed analysis of this large and data-poor basin, but the poor gauge comparisons presented in this paper have more to do with lack of evaluation data than with model inaccuracies. As the largest river in Africa, results for the Congo dominate the summed continental results presented in Figure 5.

4.3. Intra-annual Variability

[37] In addition to providing an estimate of the day of annual peak flow, STS routing allows us to compare variability of simulated discharge to gauge data on daily and seasonal timescales. In both regards, there are considerable differences between simulations included in this study. C1 yielded estimates of daily and seasonal variability that were large relative to observations for most river basins, while results for the N1 and N50+ differed among basins (Figure 3), but were similar to observations when averaged across

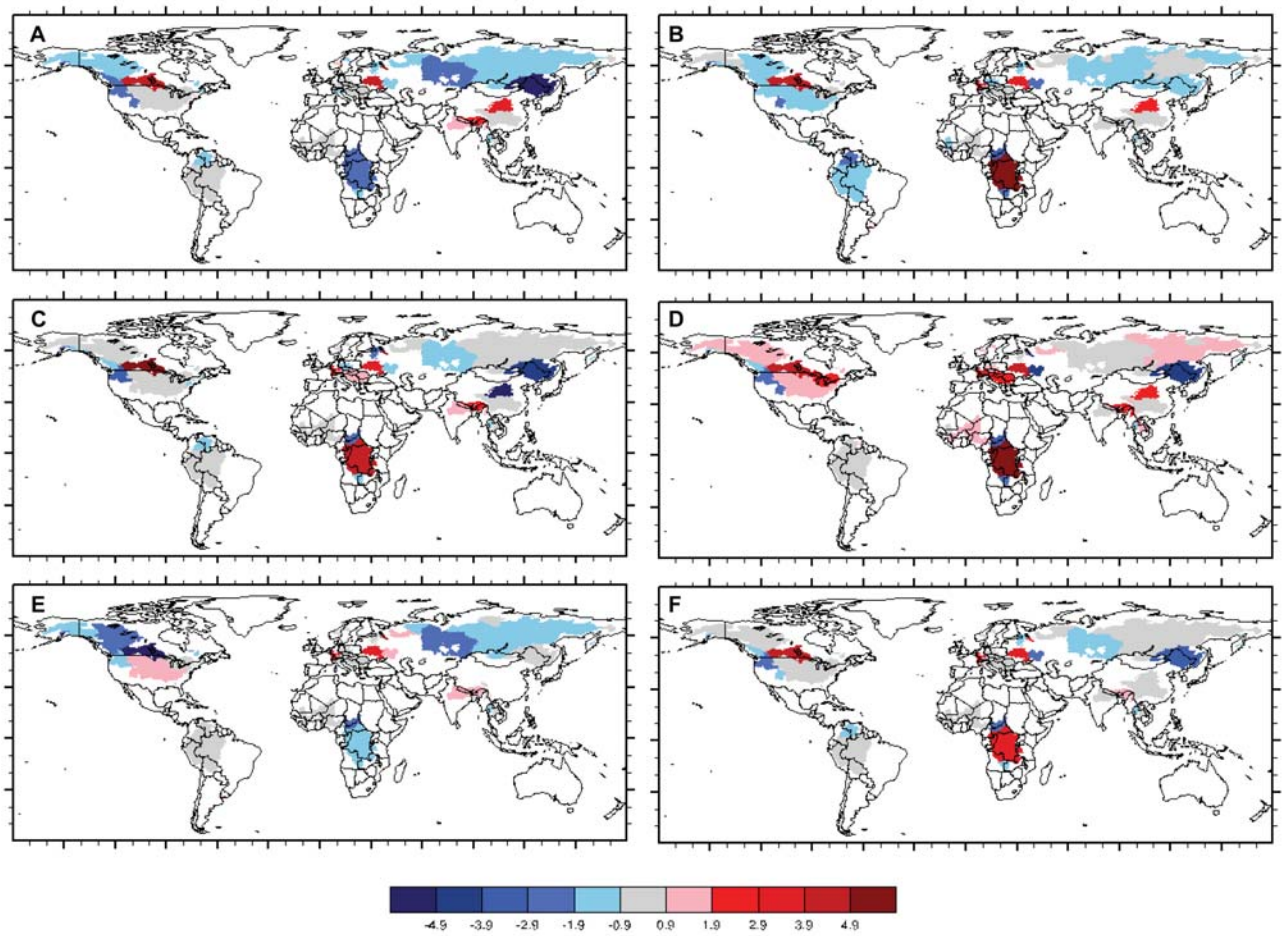

Figure 6. Difference in the climatological date of peak discharge in simulations relative to gauge data (in months). Blue colors indicate simulated peaks that are early relative to observed, red colors peaks that are late relative to observed, and shading indicates timing that is within a month of observed.

continents (Figure 5). V1 and M1 both exhibited low daily variability and a small seasonal range relative to observed discharge in the majority of basins and in the continental total for Asia and South America. Europe is the only continent for which variability in V1 and M1 exceeds variability in gauge data—a result driven by large simulated seasonal variability in Rhine River discharge that is not observed in the gauge records of this highly managed river (Figure 3). Apparently, discrepancies between modeled and observed variability are more strongly influenced by the choice of model than by any shortcomings of the routing scheme.

[38] The influence of STS routing on the variability and timing of simulated discharge can be visualized using Taylor plots. Figure 8a plots the correlation and standard deviation of summed C1 simulated daily runoff (shaded circles) and C1 routed daily discharge (black circles) relative to gauge reports for 15 of the world's largest river basins. As expected, summed distributed runoff exhibits substantially larger daily variability than gauged discharge, while routed discharge estimates exhibit variability that is on the same order as gauged variability in most basins. This result is most pronounced for rivers that include large lakes—for example, the St. Lawrence (number 14). Routed discharge also shows substantially larger correlation with daily gauge data. In addition to demonstrating the utility of the routing algorithm, the results in Figure 8a provide insight on C1 performance in various river basins. For example, we see that in the Brahmaputra basin (number 5), the C1 simulation underestimated daily variability in runoff such that no routing scheme could provide adequate estimates of discharge. For this basin, it would be necessary to scale model results or, more importantly, reinvestigate the accuracy of meteorological forcing and model parameters in the Brahmaputra region. For the Pechora River (number 20), C1 produced large estimates of daily variability, and even routed discharge was twice as variable as gauge reports. In this basin we are investigating STS routing parameters as well as meteorological data and model parameters.

[39] Figure 8b shows the annual range relative to gauge data and the correlation with gauge data for daily discharge in all five simulations for selected rivers of interest. In some rivers, including the Mississippi (number 7), the majority of models perform well by these metrics. In others, such as the Ob (number 10), there is a wide spread in simulation results. More generally, C1 tended to overestimate seasonal variability in discharge while M1 and V1 tended to underestimate variability. This is confirmed in Figures 8c and 8d, which show average results for each model for continents and for the globe, respectively. Results for Africa (Figure 8c) show the lowest accuracy and widest model range, which

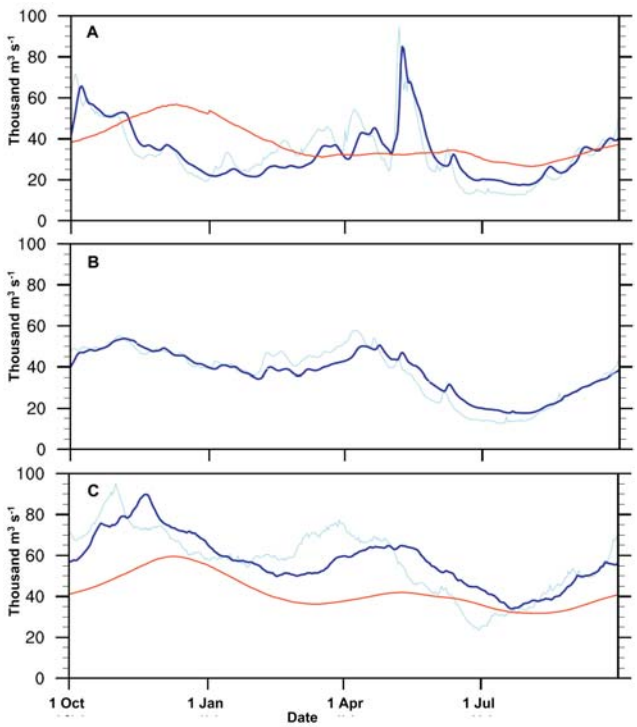

Figure 7. Climatological average hydrograph for Noah simulations of the Congo Basin. Runoff (light blue), routed simulated discharge (dark blue), and gauged discharge (red) for (a) N1 for the period of gauge record, (b) N1 for the entire 1979–2007 simulation, and (c) N50+.

traces back to the deficiency of gauge records and of observation-based knowledge of that continent. Results for Europe, Asia, and North America are more tightly clustered and are better on average. Globally, and for each continent except for Africa, the multimodel average falls within 30% of gauged seasonal variability and provides daily correlations of 0.5 or better.

4.4. Interannual Variability

[40] Simulation of interannual variability in peak discharge is a product of the combined properties of forcing data, the distributed LSM, and the routing scheme. As seen in Figure 3, simulations in this study overestimated the variability of annual peak discharge relative to observation in some major river basins and underestimated it in others. In the aggregate, simulations tended to underestimate interannual peak variability relative to gauge data in South America and to overestimate it in Europe and Africa (Figure 5). Globally, C1 produced overestimates of peak flow variability while all other simulations fell within 20% of summed observed discharge variability. C1 overestimates are a reflection of CLM2's relatively small dynamic range in soil moisture relative to other models. This small dynamic range causes the soil to saturate at lower values than is the case for other models, resulting in larger partitioning to runoff in general. Because runoff is a threshold process, this characteristic is particularly pronounced in wet years, when CLM2 produces more frequent runoff events relative to other models and particularly high simulations of peak discharge.

[41] While the magnitude of discharge peaks varies between models, the correlation between interannual peak variability in simulated discharge and gauge records is largely a function of the precipitation forcing data set. As such, the GLDAS simulations included in the study generally yielded similar results (Table 2). Somewhat lower correlations for small basins in the N50+ simulation may result from the fact that the *Sheffield et al.* [2006] data set is based on resampled daily precipitation data that may not preserve the exact dates of storms. The routing algorithm did improve the strength of correlation with gauged data for most basins relative to unrouted, summed runoff. This improvement reflects the fact that the STS scheme skillfully translates and attenuates distributed runoff from across the basin, taking into account variability in transport time, and for larger basins, that transport time from headwaters regions can exceed the calendar year, such that a year with high precipitation (and thus high distributed runoff) will lead to above-average discharge in the following year. This effect is particularly pronounced for the Amazon River. The few exceptions to STS improvement (N1 in the Congo and N1, V1, and M1 in the Mekong) result from cases in which models either failed to capture or falsely produced one or two large runoff events that dominated the correlation signal. For both of these rivers the period of gauge data is only a few years long, such that a single event can have this effect on interannual statistics.

5. Discussion

[42] It is not surprising to find substantial differences in simulated runoff among simulations which used the same meteorological forcing data but different LSMs (N1, C1, V1, and M1). Numerous multimodel studies of the Project for Intercomparison of Land Surface Parameterization Schemes [*Henderson-Sellers et al.*, 1995], the Global Soil Wetness Project [*Dirmeyer et al.*, 1999; *IGPO*, 2002], and GLDAS have found that the choice of LSM is often the dominant determinant of simulated water and energy fluxes. These studies considered multiple models, meteorological forcing data sets, spatial resolutions, and/or surface parameterizations [e.g., *Dirmeyer et al.*, 2006; *Kato et al.*, 2007; *Liang et al.*, 1998; *Lohmann et al.*, 1998]. Specifically to GLDAS, *Kato et al.* [2007] found that the choice of LSM had a substantial impact on the simulation of evapotranspiration at selected coordinated enhanced observing period (CEOP) sites. In particular, GLDAS/CLM2 tended to underestimate evapotranspiration. Our results complement that finding, as we found that CLM2 (simulation C1) generally yielded the highest estimates of runoff. Mosaic (M1) produced the least runoff and was well below gauged discharge in most cases, and Noah (N1 and N50+) and VIC (V1) also tended to underestimate runoff.

[43] Our results are also broadly consistent with earlier LSM intercomparison studies. In an analysis of the North American Land Data Assimilation System (NLDAS), *Lohmann et al.* [2004] found that Mosaic yielded high estimates of evapotranspiration and low estimates of runoff relative to Noah LSM and relative to gauge records of river discharge. In contrast to our study, *Lohmann et al.* [2004] found that VIC gave the highest estimates of runoff, but this may be explained by the fact that we used VIC in water balance mode rather than full energy balance mode.

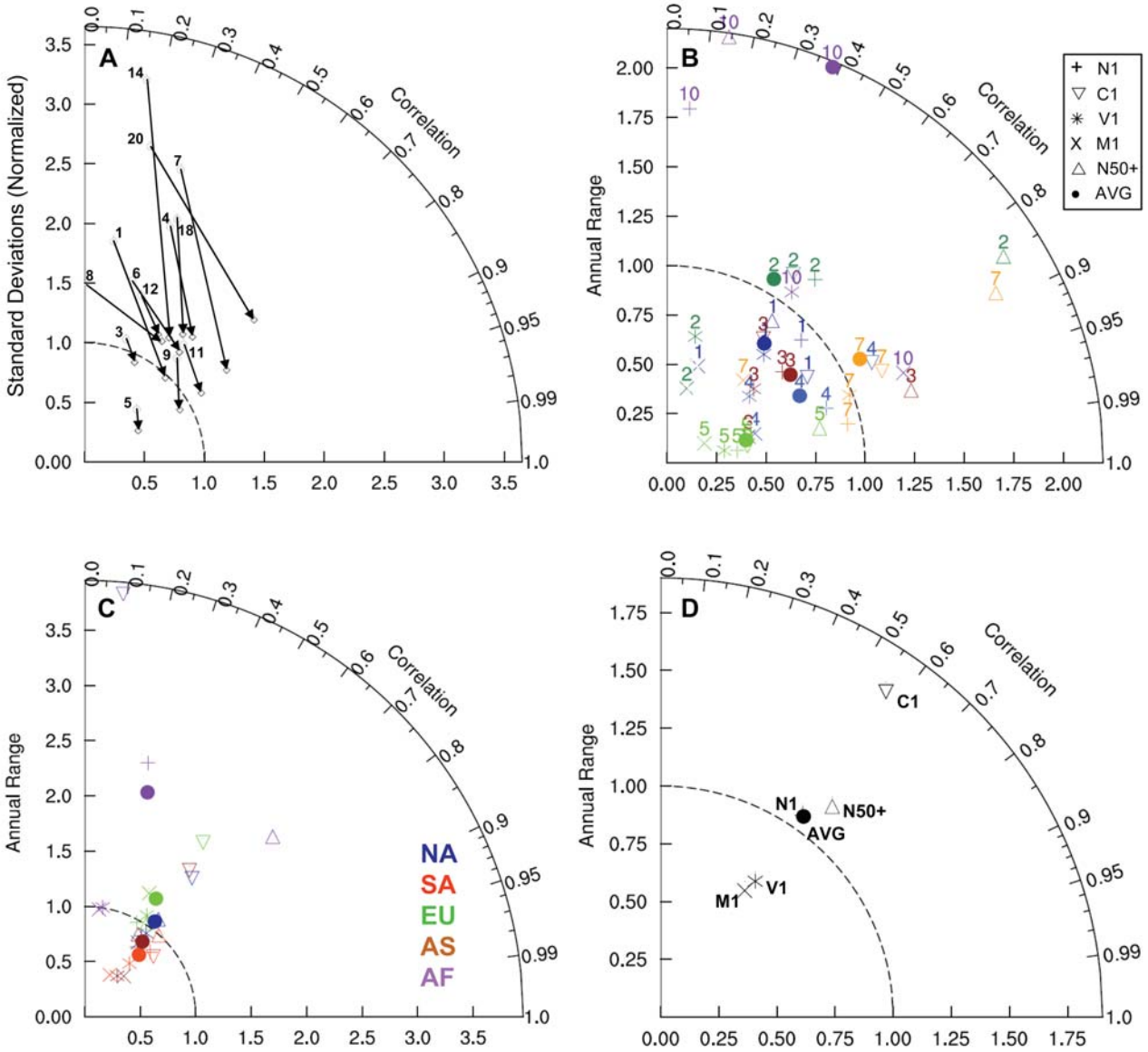

Figure 8. Taylor Plots showing: (a) the correlation and standard deviation of C1 daily summed runoff (grey circles) and daily routed discharge (black circles) for fifteen of the largest river basins included in the study, relative to gauge observations of daily discharge. Arrows connect runoff to discharge for each basin, and numbers are as listed in Figure 1. (b) Daily correlation and average seasonal variability (maximum daily flow – minimum daily flow) for selected basins of interest for each simulation and for the mean of all simulations, relative to gauge observations. (c) As in Figure 8b, but for totals over each continent. (d) As in Figure 8b, but for the total of all basins included in the study. Note that in Figure 8d, N1 falls on top of AVG.

Slater et al. [2007] applied a suite of LSMs to estimate runoff from major Arctic rivers. Four out of five LSMs included in their study underestimated mean discharge in the Yenisei, Lena, and Mackenzie rivers, while the opposite was true for the Ob River. Similarly, we found that all simulations except for C1 underestimated discharge in the Yenisei, Lena, and Mackenzie, while results for the Ob were mixed, with the multimodel mean approximately equal to observed discharge. It is noteworthy that *Slater et al.* [2007] used ERA-40 meteorological forcing data, which we did not include in our study; our similar results in these basins, then, may be related to model failure to replicate the high partitioning of precipitation into runoff that has been observed in the Yenisei and Lena [*Slater et al.*, 2007].

5.1. High-Latitude Rivers

[44] High-latitude basins exhibit a distinctive discharge peak associated with snowmelt. This peak leads to hydrographs with large annual range and a peak in late spring or early summer (Figure 1). In these basins, simulation V1 best captured the timing of the discharge peak, but both V1 and M1 yielded underestimates of total discharge and the magnitude of seasonal variability. C1 and N50+, meanwhile,

Table 2. Interannual Variability in Peak Discharge[a]

River	N1		C1		V1		M1		N50+		Avg.	
	ΣR	Q	ΣR	Q	ΣR	Q	ΣR	Q	ΣR	Q	ΣR	Q
Amazon	0.07	0.68	−0.16	0.61	0.06	0.66	0.09	0.60	0.57	0.75	0.13	0.66
Congo	0.83	0.79	0.78	0.91	0.39	0.40	0.52	0.76	0.53	0.55	0.61	0.68
Yenisey	0.28	0.29	0.55	0.68	0.13	0.15	0.28	0.34	0.26	0.28	0.30	0.35
Mississippi	0.71	0.76	0.45	0.54	0.62	0.75	0.52	0.71	0.74	0.69	0.61	0.69
Mekong	0.80	0.45	0.72	0.81	0.69	0.46	0.19	−0.18	0.62	0.61	0.60	0.43
Ganges	0.94	0.96	0.68	0.79	0.85	0.98	0.74	0.92	0.38	0.34	0.72	0.80
Mackenzie	0.39	0.41	0.40	0.49	0.14	0.13	0.32	0.34	0.40	0.45	0.33	0.37
Yukon	0.21	0.32	0.41	0.38	0.11	0.17	0.22	0.20	0.56	0.83	0.30	0.38
Kolyma	0.88	0.86	0.87	0.87	0.59	0.67	0.65	0.72	0.60	0.79	0.72	0.78
Rhine	0.54	0.54	0.32	0.55	0.30	0.48	0.34	0.37	0.44	0.49	0.39	0.49
Copper	0.60	0.66	0.76	0.73	0.59	0.60	0.52	0.61	−0.01	0.08	0.49	0.54
Po	0.76	0.75	0.56	0.91	0.49	0.68	0.58	0.75	0.72	0.86	0.62	0.79
Glama	0.42	0.56	0.56	0.70	0.67	0.70	0.68	0.66	0.42	0.51	0.55	0.62
Connecticut	0.50	0.71	0.38	0.68	0.36	0.62	0.33	0.44	0.29	0.28	0.37	0.55
Colorado	0.55	0.73	0.33	0.46	0.59	0.62	0.21	0.28	0.15	0.26	0.37	0.47
All	0.57	0.63	0.51	0.67	0.44	0.54	0.41	0.50	0.44	0.52	0.47	0.57

[a]Correlation between GRDC gauged discharge and ΣR, basin-summed daily simulated runoff, and Q, the GLDAS-STS simulated daily discharge, for the same selected basins listed in Table 2. The multimodel average correlations for each river are also shown, as are the (unweighted) average for all rivers included in the table.

provided the most accurate simulations of the magnitude of mean annual discharge, but both tended to melt snow too early in the spring, leading to erroneously early peaks in simulated river discharge. The V1 results suggest that the VIC snowmelt scheme performs well for these regions of deep seasonal snowpack, as has been shown in previous studies [e.g., *Pan et al.*, 2003; *Sheffield et al.*, 2003; *Su et al.*, 2006], but that the V1 simulation of runoff suffers from a dry bias—either the GLDAS precipitation forcing data set underrepresents runoff-inducing events or VIC parameterizations systematically cause underestimates of runoff in partitioning the local water balance. Given that precipitation data sets suffer from a scarcity of observations at high latitudes and typically underestimate snowfall and alpine precipitation (in part due to gauge undercatch, which is not directly addressed for gauge data used in CMAP), we can speculate that the precipitation forcing may be the culprit here. The situation is similar for M1, which also produces small discharge peaks relative to observed discharge that are reasonably accurate in their timing. The N50+ and N1 results suggest that Noah version 2.7 has a tendency to melt the seasonal snowpack prematurely. This was a known model development issue in Noah for some time and has been a focus of recent experimental model updates. N50+ yields slightly more accurate estimates of mean annual discharge for high-latitude basins, suggesting that the combination of Noah v2.7 with the *Sheffield et al.* [2006] forcing provides better representations of high-latitude hydrology than Noah version 2.7 forced with the standard GLDAS meteorological data sets. The C1 results for high-latitude basins indicate that there is a slight tendency toward premature snowmelt in CLM2, though results varied between basins. C1 results for mean annual discharge and seasonal variability indicate that the combination of CLM2 and standard GLDAS meteorological forcing is effective for high-latitude basins. In the context of our other results, however, it seems that this effective combination is actually a fortuitous product of offsetting biases: the CMAP tendency to give low estimates of precipitation balances CLM2's tendency to overestimate runoff on account of the relatively small dynamic soil moisture range in that model.

5.2. Midlatitude Rivers

[45] Results for midlatitude river basins were less consistent than for high-latitude basins, reflecting the diverse processes that influence the generation of runoff across these latitudes. In both North America and Asia, the C1 and N50+ simulations tended to produce reasonable estimates of mean annual discharge and seasonal variability while V1, M1, and N1 tended to show less total discharge and seasonal variability than gauge data. Europe was an exception in this regard, as both C1 and N50+ appear to overestimate discharge while V1, M1, and N1 are more similar to gauge reports. Simulations of the timing of peak discharge were mixed between models and across different regions. Overall, the multimodel average tended to outperform any single model, though timing results are particularly difficult to evaluate in midlatitude rivers due to water management: the STS parameters used in this study accounted for large reservoirs but not for smaller reservoirs or active water management, so our evaluation of the results in intensely managed river basins is limited. This limitation can be addressed in future studies by performing more detailed parameterization in selected river basins of interest, or alternatively, by evaluating STS results against naturalized streamflow data [e.g., *Maurer et al.*, 2002]. Evaluation at midlatitudes also suffered from a shortage of daily discharge data from most major rivers in the semi-arid regions of the Middle East and Central Asia. The underrepresentation of these river basins in global, publicly available hydrological databases is a perpetual obstacle for studies of climate and water resources in these critically water-stressed regions.

5.3. Tropical Rivers

[46] Simulations N1, C1, V1, and M1 all underestimated discharge in the Amazon and Orinoco, while N50+ provided reasonable estimates. This result strongly suggests that the GLDAS (CMAP) precipitation data underestimate precipitation in tropical South America. Allowing for this underestimate, however, N1 and C1 did provide reasonably accurate simulations of the timing of peak discharge and of seasonal variability. Interannual variability was underestimated for the Amazon but estimated accurately for the

Orinoco in all simulations. Results for tropical rivers of Africa and Asia were mixed. In Africa, N50+ tended to yield the best estimates of peak discharge timing, a result that benefits from a longer period of gauge comparison than was available for GLDAS, while N1 tended to be closest in the simulation of mean annual discharge and V1 and M1 yielded the best estimates of seasonal variability. C1 and N50+ overestimated discharge and seasonal variability. All models overestimated interannual variability in the large African rivers, indicating the need for more reliable precipitation records in many of these basins. Results for large African basins are particularly difficult to assess given the complex hydrology of these rivers: the Niger River has a large internal delta that influences evaporation, groundwater interaction, and flow velocity in ways that are probably not fully captured by the STS parameterization, while the Congo has a bimodal seasonal hydrograph and limited evaluation data.

[47] In Asia, all simulations underestimated mean annual discharge and interannual variability for the Mekong River, but C1, N1, and N50+ provided good estimates of daily variability, seasonal variability, and timing of peak flow. Similar patterns held for the Brahmaputra and Irrawaddy, where models tended to underestimate mean discharge but captured timing, and in some cases, seasonal and subseasonal variability. In the Ganges and Chao Phraya, simulations provided mixed results; as in other regions, C1 and N50+ produced the highest discharge estimates and V1 and M1 were dry relative to gauge observations. These geographical differences in model performance within tropical Asia indicate that a more detailed assessment of precipitation forcing data is required. All of these rivers are dominated by the signal of the Asian monsoon, but their headwaters regions are affected by the monsoon in different ways. More accurate representation of the volume, timing, and spatial distribution of monsoon precipitation is critical for hydrological analysis and prediction in these basins.

6. Conclusions

[48] A simple, computationally efficient source-to-sink (STS) routing scheme was applied to the Global Land Data Assimilation System (GLDAS). The routing scheme requires minimal parameterization and can be applied as a post-processor to large inventories of distributed runoff data of the type generated by global climate models, reanalyses, and offline LSM simulations. Parameters for the scheme were estimated using previously published methods, and the behavior of the routing system was physically reasonable for all basins.

[49] Applying STS to GLDAS runoff fields provides a method for assessing GLDAS hydrology in regions with limited observations of distributed hydrological fluxes. These assessments are in no sense a complete evaluation of model performance, but they yield useful insights on the differing behaviors of various LSMs and the confidence that we can place in their ability to simulate water cycle processes under differing geographies and climate conditions. For example, the results of this study clearly indicate that over much of the globe the combination of standard GLDAS forcing with the Mosaic and VIC LSMs (as currently implemented in GLDAS) yield simulations that significantly underestimate runoff. The comparison of standard GLDAS forcing with the long-term forcing data set of *Sheffield et al.* [2006], meanwhile, indicates that Noah version 2.7 with standard GLDAS forcing yields lower estimates of runoff than Noah version 2.7 with *Sheffield et al.* [2006] forcing, and that results with *Sheffield et al.* [2006] forcing tend to more closely resemble observed discharge. This encourages us to perform further experiments with the *Sheffield et al.* [2006] forcing, as both VIC and Mosaic will likely yield better results with this data set. At the same time, the study suggests that GLDAS precipitation may suffer from a dry bias in a number of important regions, and this will need to be investigated. The study also indicates that V1 was generally quite accurate in estimating the timing of peak discharge, while M1 peaks were late relative to gauge observations in the majority of midlatitude and high-latitude basins. In part, these results reflect known characteristics of these LSMs: VIC was designed for hydrological application and has been tested repeatedly against river discharge estimates, while Mosaic has a known tendency to retain water, leading to high estimates of soil moisture and evapotranspiration relative to other models. Forcing data may also play a role in these results, and this will be explored in future studies.

[50] For simulations that use the standard GLDAS forcing, this study indicates that CLM2 provides the most realistic simulations of mean annual runoff, a result that may, in many basins, be the product of an offset between a dry precipitation bias in GLDAS and a small dynamic range of soil moisture in CLM2. However, Noah, VIC, and, to a lesser degree, Mosaic, provide better simulations of seasonal and interannual variability in many cases. Simulation of peak discharge timing varied between models and regions, with a multimodel average frequently yielding the most reliable estimate. The selection of the "best" model or combination of models for any given application, then, depends on the region of interest and scientific goal of the study. In addition, future GLDAS-STS studies will investigate the sensitivity of simulated discharge to parameterizations of convective precipitation and to the frequency and spatial resolution of meteorological forcing data: these factors are expected to have a considerable impact on the simulation of runoff in any offline LSM.

[51] Finally, it must be noted that this was a global study, and that STS parameters will require further refinement in many basins. For example, the current parameterization does not include seasonal variability in river velocity or subseasonal variability in rates of direct evaporation. The STS parameters also fail to account for small reservoirs or active dam management, and the complex hydrology of inland deltas and seasonal wetlands demand further attention. Some of these factors will be included in future refinements of the global STS presented in this paper, while others are more appropriately addressed in regional or watershed-scale applications. We anticipate that the simplicity, scalability, and computational efficiency of the STS algorithm will encourage multiple independent efforts to improve and customize the routing system.

[52] **Acknowledgments.** The authors thank Hiroko Kato for performing the GLDAS simulations used in this study and for providing insight on their results. The authors also thank multiple members of the NASA Hydrological Sciences Branch for contributing their ideas and technical expertise. The Global Runoff Data Center (GRDC) is gratefully acknowledged for providing all river gauge data used in this study. This

work was funded by NASA's Energy and Water Cycle Study (NEWS) program.

References

Arora, V. K., and G. J. Boer (1999), A variable velocity flow routing algorithm for GCMs, *J. Geophys. Res.*, *104*(D24), 30,965–30,979, doi:10.1029/1999JD900905.

Arora, V. K., F. H. S. Chiew, and R. B. Grayson (1999), A river flow routing scheme for general circulation models, *J. Geophys. Res.*, *104*(D12), 14,347–14,357, doi:10.1029/1999JD900200.

Avissar, R., and R. A. Pielke (1989), A parameterization of heterogeneous land surfaces for atmospheric numerical-models and its impact on regional meteorology, *Mon. Weather Rev. 117*(10), 2113–2136, doi:10.1175/1520-0493(1989)117<2113:APOHLS>2.0.CO;2.

Bell, V. A., A. L. Kay, R. G. Jones, and R. J. Moore (2007), Development of a high-resolution grid-based river flow model for use with regional climate model output, *Hydrol. Earth Syst. Sci.*, *11*(1), 532–549.

Bonan, G. B. (1998), The land surface climatology of the NCAR land surface model coupled to the NCAR community climate model, *J. Clim.*, *11*(6), 1307–1326, doi:10.1175/15200442(1998)011<1307:TLSCOT>2.0.CO;2.

Chen, F., K. Mitchell, J. Schaake, Y. K. Xue, H. L. Pan, V. Koren, Q. Y. Duan, M. Ek, and A. Betts (1996), Modeling of land surface evaporation by four schemes and comparison with FIFE observations, *J. Geophys. Res.*, *101*(D3), 7251–7268, doi:10.1029/95JD02165.

Cherkauer, K. A., and D. P. Lettenmaier (1999), Hydrologic effects of frozen soils in the upper Mississippi River basin, *J. Geophys. Res.*, *104*(D16), 19,599–19,610, doi:10.1029/1999JD900337.

Coe, M. T. (1997), Simulating continental source waters: An application to Holocene Northern Africa, *J. Clim.*, *10*(7), 1680–1689, doi:10.1175/1520-0442(1997)010<1680:SCSWAA>2.0.CO;2.

Coe, M. T. (2000), Modeling terrestrial hydrological systems at the continental scale: Testing the accuracy of an atmospheric GCM, *J. Clim.*, *13*(4), 686–704, doi:10.1175/1520-0442(2000)013<0686:MTHSAT>2.0.CO;2.

Costa, M. H., and J. A. Foley (1997), Water balance of the Amazon Basin: Dependence on vegetation cover and canopy conductance, *J. Geophys. Res.*, *102*(D20), 23,973–23,989, doi:10.1029/97JD01865.

Dai, A., and K. E. Trenberth (2002), Estimates of freshwater discharge from continents: Latitudinal and seasonal variations, *J. Hydrometeorol.*, *3*, 660–686, doi:10.1175/1525-7541(2002)003<0660:EOFDFC>2.0.CO;2.

Dai, Y., and Q. Zeng (1997), A land surface model (IAP94) for climate studies, Part I: Formulation and validation in off-line experiments, *Adv. Atmos. Sci.*, *14*, 443–460.

Dai, Y., et al. (2003), The common land model, *Bull. Am. Meteorol. Soc.*, *84*, 1013–1023, doi:10.1175/BAMS-84-8-1013.

Decharme, B., H. Douville, C. Prigent, F. Papa, and F. Aires (2008), A new river flooding scheme for global climate applications: Off-line evaluation over South America, *J. Geophys. Res.*, *113*, D11110, doi:10.1029/2007JD009376.

Derber, J. C., D. F. Parrish, and S. J. Lord (1991), The new global operational analysis system at the National Meteorological Center, *Weather Forecast.*, *6*, 538–547, doi:10.1175/1520-0434(1991)006<0538:TNGOAS>2.0.CO;2.

Dickinson, R. E., A. Henderson-Sellers, and P. J. Kennedy (1993), Biosphere atmosphere transfer scheme (BATS) version Ie as coupled to the NCAR community climate model, in *NCAR Tech. Note, TN-387 + STR*, pp. 72.

Dingman, S. L. (2001), *Physical Hydrology*, Prentice Hall, Englewood Cliffs, NJ.

Dirmeyer, P. A., A. J. Dolman, and N. Sato (1999), The global soil wetness project: A pilot project for global land surface modeling and validation, *Bull. Am. Meteorol. Soc.*, *80*, 851–878, doi:10.1175/1520-0477(1999)080<0851:TPPOTG>2.0.CO;2.

Dirmeyer, P. A., X. Gao, M. Zhao, Z. Guo, T. Oki, and N. Hanasaki (2006), The second global soil wetness project (GSWP-2), Multi-model analysis and implications for our perception of the land surface, *Bull. Am. Meteorol. Soc.*, *87*, 1381–1397, doi:10.1175/BAMS-87-10-1381.

Ducharne, A., C. Golaz, E. Leblois, K. Laval, J. Polcher, E. Ledoux, and G. de Marsily (2003), Development of a high-resolution runoff routing model, calibration, and application to assess runoff from the LMD GCM, *J. Hydrol. Amsterdam*, *280*(1–4), 207–228, doi:10.1016/S0022-1694(03)00230-0.

Ek, M. B., K. E. Mitchell, Y. Lin, E. Rogers, P. Grunmann, V. Koren, G. Gayno, and J. D. Tarpley (2003), Implementation of Noah land surface model advances in the National Centers for Environmental Prediction operational mesoscale Eta model, *J. Geophys. Res.*, *108*(D22), 8851, doi:10.1029/2002JD003296.

Fekete, B. M., C. J. Vorosmarty, and W. Grabs (2002), High-resolution fields of global runoff combining observed river discharge and simulated water balances, *Global Biogeochem. Cycles*, *16*(3), 1042, doi:10.1029/1999GB001254.

Gottschalck, J., J. Meng, M. Rodell, and P. Houser (2005), Analysis of multiple precipitation products and preliminary assessment of their impact on global land data assimilation system land surface states, *J. Hydrometeorol.*, *6*(5), 573–598, doi:10.1175/JHM437.1.

Graham, S. T., J. S. Famiglietti, and D. R. Maidment (1999), Five minute, 1/2 degree, and 1 degree data sets of continental watersheds and river networks for use in regional and global hydrologic and climate system modeling studies, *Water Resour. Res.*, *35*(2), 583–587, doi:10.1029/1998WR900068.

Hansen, M. C., R. S. Defries, J. R. G. Townshend, and R. Sohlberg (2000), Global land cover classification at 1 km spatial resolution using a classification tree approach, *Int. J. Remote Sens.*, *21*(6–7), 1331–1364, doi:10.1080/014311600210209.

Henderson-Sellers, A., A. Pitman, P. Love, P. Irannejad, and T. Chen (1995), The project for intercomparison of land-surface parameterization schemes (PILPS): Phases 2 and 3, *Bull. Am. Meteorol. Soc.*, *94*, 489–503, doi:10.1175/1520-0477(1995)076<0489:TPFIOL>2.0.CO;2.

IGPO (2002), 2: The second global soil wetness project science and implementation plan, in *IGPO Publ. Ser. 37*, 65 pp., GSWP, Silver Spring, MD.

Kato, H., M. Rodell, F. Beyrich, H. Cleugh, E. van Gorsel, H. Z. Liu, and T. P. Meyers (2007), Sensitivity of land surface simulations to model physics, land characteristics, and forcings, at four CEOP sites, *J. Meteorol. Soc. Jpn.*, *85A*, 187–204, doi:10.2151/jmsj.85A.187.

Kopp, T. J., and R. B. Kiess (1996), The Air Force Global Weather Central cloud analysis model, in *AMS 15th Conf. on Weather Analysis and Forecasting*, pp. 220–222, Norfolk, VA.

Koren, V., J. Schaake, K. Mitchell, Q. Y. Duan, F. Chen, and J. M. Baker (1999), A parameterization of snowpack and frozen ground intended for NCEP weather and climate models, *J. Geophys. Res.*, *104*(D16), 19,569–19,585, doi:10.1029/1999JD900232.

Koster, R. D., and M. J. Suarez (1996), Energy and water balance calculations in the Mosaic LSM, *NASA Tech. Memo.*, *104606*, 76 pp.

Koster, R. D., M. J. Suarez, P. Liu, U. Jambor, M. Kistler, A. Berg, R. Reichle, M. Rodell, and J. Famiglietti (2004), Realistic initialization of land surface states: Impacts on subseasonal forecast skill, *J. Hydrometeorol.*, *5*(6), 1049–1063, doi:10.1175/JHM-387.1.

Kumar, S. V., et al. (2006), Land information system: An interoperable framework for high-resolution land surface modeling, *Environ. Model. Softw.*, *21*(10), 1402–1415, doi:10.1016/j.envsoft.2005.07.004.

Leopold, L. B., M. G. Wolman, and J. P. Miller (1964), Fluvial Processes in Geomorphology, W.H. Freeman, New York.

Liang, X., E. F. Wood, and D. P. Lettenmaier (1996), Surface soil moisture parameterization of the VIC-2L model: Evaluation and modification, *Global Planet. Change*, *13*(1–4), 195–206, doi:10.1016/0921-8181(95)00046-1.

Liang, X., D. Lettenmaier, E. F. Wood, and S. J. Burges (1994), A simple hydrologically based model of land surface water and energy fluxes for GSMs, *J. Geophys. Res.*, *99*(D7), 14,415–14,428, doi:10.1029/94JD00483.

Liang, X., et al. (1998), The Project for intercomparison of land-surface parameterization schemes (PILPS) phase 2(c) Red-Arkansas River basin experiment: 2. Spatial and temporal analysis of energy fluxes, *Global Planet. Change*, 19, 137–159, doi:10.1016/S0921-8181(98)00045-9.

Liston, G. E., Y. C. Sud, and E. F. Wood (1994), Evaluating Gcm land-surface hydrology parameterizations by computing river discharges using a runoff routing model —application to the Mississippi Basin, *J. Appl. Meteorol.*, *33*(3), 394–405, doi:10.1175/1520-0450(1994)033<0394:EGLSHP>2.0.CO;2.

Lohmann, D., R. Nolte-Holube, and E. Raschke (1996), A large-scale routing model to be coupled to land surface parameterizations schemes, *Tellus, Ser. A*, *48*, 708–721, doi:10.1034/j.1600-0870.1996.t01-3-00009.x.

Lohmann, D., et al. (1998), The project for intercomparison of land-surface parameterization schemes (PILPS) phase 2(c) Red-Arkansas River basin experiment: 3. Spatial and temporal analysis of water fluxes, *Global Planet. Change*, *19*, 161–179, doi:10.1016/S0921-8181(98)00046-0.

Lohmann, D., et al. (2004), Streamflow and water balance intercomparisons of four land surface models in the North American Land Data Assimilation System project, *J. Geophys. Res.*, *109*, D07S91, doi:10.1029/2003JD003517.

Maurer, E. P., A. W. Wood, J. C. Adam, D. P. Lettenmaier, and B. Nijssen (2002), A long-term hydrologically based data set of land surface fluxes and states for the conterminous United States, *J. Clim.*, *15*, 3237–3251, doi:10.1175/1520-0442(2002)015<3237:ALTHBD>2.0.CO;2.

Mesa, O. J., and E. R. Mifflin (1986), On the relative role of hillslope and network geometry in hydrologic response, in *Scale Problems in Hydrology*, edited by V. K. Gupta, I. Rodriguez-Iturbe, E. F. Wood, and D. Reidel, pp. 1–17, Norwell, Mass.

Miller, J. R., G. L. Russell, and G. Caliri (1994), Continental-scale river flow in climate models, *J. Clim.*, *7*(6), 914–928, doi:10.1175/1520-0442(1994)007<0914:CSRFIC>2.0.CO;2.

Mitchell, K. E., et al. (2004), The multi-institution North American Land Data Assimilation System (NLDAS): Utilizing multiple GCIP products and partners in a continental distributed hydrological modeling system, *J. Geophys. Res.*, *109*, D07S90, doi:10.1029/2003JD003823.

Monteith, J. L. (1981), Evaporation and surface temperature, *Q. J. R. Meteorol. Soc.*, *107*, 1–27, doi:10.1256/smsqj.45101.

Naden, P. S. (1992), Spatial variability in flood estimation for large catchments: The exploitation of channel network structure, *J. Hydrol. Sci.*, *37*, 53–71, doi:10.1080/02626669209492561.

Naden, P. S. (1993), A routing model for continental-scale hydrology, in *Macroscale Modeling of the Hydrosphere, Proceedings of the Yokohama Symposium, July 1993*, pp. 67–79, IAHS, Oxfordshire, UK.

Ngo-Duc, T., J. Polcher, and K. Laval (2005), A 53 year forcing data set for land surface models, *J. Geophys. Res.*, *110*, D06116, doi:10.1029/2004JD005434.

Ngo-Duc, T., T. Oki, and S. Kanae (2007), A variable streamflow velocity method for a global river routing model: Model description and preliminary results, *Hydrol. Earth Syst. Sci. Discuss.*, *4*, 4389–4414.

Nijssen, B., D. P. Lettenmaier, X. Liang, S. W. Wetzel, and E. F. Wood (1997), Streamflow simulation for continental-scale river basins, *Water Resour. Res.*, *33*(4), 711–724, doi:10.1029/96WR03517.

Nijssen, B., et al. (2003), Simulation of high-latitude hydrological processes in the Torne-Kalix basin: PILPS phase 2(e)—2: Comparison of model results with observations, *Global Planet. Change*, *38*(1–2), 31–53, doi:10.1016/S0921-8181(03)00004-3.

Oki, T., and Y. C. Sud (1998), Design of total runoff integrating pathways (TRIP), *Earth Interact.*, *2*, 1–36, doi:10.1175/1087-3562(1998)002<0001:DOTRIP>2.3.CO;2.

Oki, T., T. Nishimura, and P. Dirmeyer (1999), Assessment of annual runoff from land surface models using total runoff integrating pathways (TRIP), *J. Meteorol. Soc. Jpn.*, *77*, 235–255.

Olivera, F., and D. Maidment (1999), GIS-based spatially distributed model for runoff routing, *Water Resour. Res.*, *35*(4), 1155–1164.

Olivera, F., and S. Koka (2004), Advective and hydrodynamic dispersive processes in watershed response, *J. Hydrol. Eng.*, *9*(6), 534–544, doi:10.1061/(ASCE)1084-0699(2004)9:6(534).

Olivera, F., J. Famiglietti, and K. Asante (2000), Global-scale flow routing using a source-to-sink algorithm, *Water Resour. Res.*, *36*(8), 2197–2207, doi:10.1029/2000WR900113.

Pan, M., et al. (2003), Snow process modeling in the North American Land Data Assimilation System (NLDAS): 2. Evaluation of model simulated snow water equivalent, *J. Geophys. Res.*, *108*(D22), 8850, doi:10.1029/2003JD003994.

Penman, H. L. (1948), Natural evaporation from open water, bare soil, and grass, *Proc. R. Soc. London, Ser. A*, *193*, 120–145, doi:10.1098/rspa.1948.0037.

Rodell, M., and P. R. Houser (2004), Updating a land surface model with MODIS-derived snow cover, *J. Hydrometeorol.*, *5*, 1064–1075.

Rodell, M., et al. (2004), The global land data assimilation system, *Bull. Am. Meteorol. Soc.*, *85*(3), 381–394, doi:10.1175/BAMS-85-3-381.

Rodell, M., P. R. Houser, A. Berg, and J. S. Famiglietti (2005), Evaluation of ten methods for initializing a land surface model, *J. Hydrometeorol.*, *6*(2), 146–155, doi:10.1175/JHM414.1.

Sausen, R., S. Schubert, and L. Dumenil (1994), A model of river runoff for use in coupled atmosphere ocean models, *J. Hydrol. Amsterdam*, *155*(3–4), 337–352, doi:10.1016/0022-1694(94)90177-5.

Schultze, K., M. Hunger, and P. Doll (2005), Simulating river flow velocity on global scale, *Adv. Geosci.*, *5*, 133–136.

Sellers, P. J., Y. Mintz, Y. C. Sud, and A. Dalcher (1986), A simple biosphere model (Sib) for use within general-circulation models, *J. Atmos. Sci.*, *43*(6), 505–531, doi:10.1175/1520-0469(1986)043<0505:ASBMFU>2.0.CO;2.

Sheffield, J., et al. (2003), Snow process modeling in the North American Land Data Assimilation System (NLDAS): 1. Evaluation of model-simulated snow cover extent, *J. Geophys. Res.*, *108*(D22), 8849, doi:10.1029/2002JD003274.

Sheffield, J., G. Goteti, and E. F. Wood (2006), Development of a 50 year high-resolution global data set of meteorological forcings for land surface modeling, *J. Clim.*, *19*, 3088–3111, doi:10.1175/JCLI3790.1.

Slater, A. G., T. J. Bohn, J. L. McCreight, M. C. Serreze, and D. P. Lettenmaier (2007), A multimodel simulation of pan-Arctic hydrology, *J. Geophys. Res.*, *112*, G04S45, doi:10.1029/2006JG000303.

Su, F., J. C. Adam, K. E. Trenberth, and D. P. Lettenmaier (2006), Evaluation of surface water fluxes of the pan-Arctic land region with a land surface model and ERA-40 reanalysis, *J. Geophys. Res.*, *111*, D05110, doi:10.1029/2005JD006387.

Syed, T. H., J. S. Famiglietti, M. Rodell, J. L. Chen, and C. R. Wilson (2008), Analysis of terrestrial water storage changes from GRACE and GLDAS, *Water Resour. Res.*, *44*, W02433, doi:10.1029/2006WR005779.

Troch, P. A., J. A. Smith, E. F. Wood, and F. P. de Troch (1994), Hydrologic controls of large floods in a small basin, *J. Hydrol. Amsterdam*, *156*, 285–309, doi:10.1016/0022-1694(94)90082-5.

Verdin, K. L., and J. Verdin (1999), A topological system for the delineation and codification of the Earth's river basins, *J. Hydrol. Amsterdam*, *218*, 1–12, doi:10.1016/S0022-1694(99)00011-6.

Voisin, N., A. W. Wood, and D. P. Lettenmaier (2008), Evaluation of precipitation products for global hydrological prediction, *J. Hydrometeorol.*, *9*(3), 388–407, doi:10.1175/2007JHM938.1.

Vorosmarty, C. (2001), Global water data: A newly endangered species, *Eos Trans. AGU*, *82*(5), 56–58, doi:10.1029/01EO00031.

Vorosmarty, C. J., B. Moore III, A. L. Grace, M. P. Gildea, J. M. Melillo, B. J. Peterson, E. B. Rastetter, and P. A. Steudler (1989), Continental scale models of water balance and fluvial transport: An application to South America, *Global Biogeochem. Cycles*, *3*, 241–265, doi:10.1029/GB003i003p00241.

Xie, P. P., and P. A. Arkin (1997), Global precipitation: A 17 year monthly analysis based on gauge observations, satellite estimates, and numerical model outputs, *Bull. Am. Meteorol. Soc. 78*(11), 2539–2558, doi:10.1175/1520-0477(1997)078<2539:GPAYMA>2.0.CO;2.

Zagona, E. A., T. J. Fulp, R. Shane, T. Magee, and H. M. Goranflo (2001), RiverWare: A generalized tool for complex reservoir systems modeling, *J. Am. Water Resour. Assoc.*, *37*(4), 913–929, doi:10.1111/j.1752-1688.2001.tb05522.x.

Zaitchik, B. F., and M. Rodell (2009), Forward-looking assimilation of MODIS-derived snow covered area into a land surface model, *J. Hydrometeorol.*, *10*(1), 130–148, doi:10.1175/2008JHM1042.1.

Zhang, J., W.-C. Wang, and J. Wei (2008), Assessing land-atmosphere coupling using soil moisture from the Global Land Data Assimilation System and observational precipitation, *J. Geophys. Res.*, *113*, D17119, doi:10.1029/2008JD009807.

F. Olivera, Zachry Department of Civil Engineering, Texas A&M University, 3136 TAMU College Station, TX 77843, USA.

M. Rodell, NASA Goddard Space Flight Center, Code 130, Greenbelt, MD 20771, USA.

B. F. Zaitchik, Department of Earth and Planetary Sciences, Johns Hopkins University, 301 Olin Hall, 3400 North Charles St., Baltimore, MD 21218, USA. (zaitchik@jhu.edu)